

## RESEARCH ARTICLE

10.1002/2014JC009791

## Key Points:

- River geometry sets the limit of applicability of classical harmonic analysis
- Response to forcing in tidal rivers is spatially and frequency dependent
- Frictional damping eventually overcomes the nonlinear generation of overtides

## Correspondence to:

P. Matte,  
pascal.matte@ete.inrs.ca

## Citation:

Matte, P., Y. Secretan, and J. Morin (2014), Temporal and spatial variability of tidal-fluvial dynamics in the St. Lawrence fluvial estuary: An application of nonstationary tidal harmonic analysis, *J. Geophys. Res. Oceans*, 119, 5724–5744, doi:10.1002/2014JC009791.

Received 6 JAN 2014

Accepted 11 AUG 2014

Accepted article online 14 AUG 2014

Published online 3 SEP 2014

## Temporal and spatial variability of tidal-fluvial dynamics in the St. Lawrence fluvial estuary: An application of nonstationary tidal harmonic analysis

Pascal Matte<sup>1</sup>, Yves Secretan<sup>1</sup>, and Jean Morin<sup>2</sup>

<sup>1</sup>Centre Eau Terre Environnement, Institut National de la Recherche Scientifique, Quebec, Canada, <sup>2</sup>Hydrology and Ecohydraulic Section, Environment Canada, Meteorological Service of Canada, Quebec, Canada

**Abstract** Predicting tides in upstream reaches of rivers is a challenge, because tides are highly nonlinear and nonstationary, and accurate short-time predictions of river flow are hard to obtain. In the St. Lawrence fluvial estuary, tide forecasts are produced using a one-dimensional model (ONE-D), forced downstream with harmonic constituents, and upstream with daily discharges using 30 day flow forecasts from Lake Ontario and the Ottawa River. Although this operational forecast system serves its purpose of predicting water levels, information about nonstationary tidal-fluvial processes that can be gained from it is limited, particularly the temporal changes in mean water level and tidal properties (i.e., constituent amplitudes and phases), which are function of river flow and ocean tidal range. In this paper, a harmonic model adapted to nonstationary tides, NS\_TIDE, was applied to the St. Lawrence fluvial estuary, where the time-varying external forcing is directly built into the tidal basis functions. Model coefficients from 13 analysis stations were spatially interpolated to allow tide predictions at arbitrary locations as well as to provide insights into the spatiotemporal evolution of tides. Model hindcasts showed substantial improvements compared to classical harmonic analyses at upstream stations. The model was further validated by comparison with ONE-D predictions at a total of 32 stations. The slightly lower accuracy obtained with NS\_TIDE is compensated by model simplicity, efficiency, and capacity to represent stage and tidal variations in a very compact way and thus represents a new means for understanding tidal rivers.

### 1. Introduction

Tides in rivers are the result of nonlinear interactions of the oceanic tide with channel geometry, bottom friction, and river flow. They are best represented by a diffusive phenomenon in which the tidal wave, originating from tidal forces in the ocean, is increasingly distorted and damped as it propagates upriver [LeBlond, 1978]. This results in asymmetries in the duration of ebb and flood, as well as in the timing and height of high and low water [Godin, 1984, 1999; Nidziko, 2010]. Fortnightly oscillations of mean water levels (MWL) following the neap-spring cycle also increase in strength upstream and eventually surpass the semidiurnal tidal amplitude, with mean low water progressively being lowered during neap tides rather than spring tides [LeBlond, 1979, 1991; Gallo and Vinzon, 2005].

Classical harmonic analysis (HA) is possibly the most widely used approach to analyze and predict tides. It performs very well in semiencllosed basins, coastal shelves, and seas, but usually fails in representing river tides, as the assumptions of stationarity and independence of the tidal components are not fulfilled due to nontidal modulating processes [Jay and Flinchem, 1999]. As a consequence, no information on the evolution of the tidal content in time as a function of the nontidal forcing (e.g., annual river flow cycle) can be extracted. Some authors [e.g., Godin, 1985; Jay and Flinchem, 1997; Godin, 1999] showed the potential of simple regression relations to predict the modification of the tide by variations in river flow, but most investigators have turned to numerical modeling in order to get around the problem of nonstationary signals (i.e., tidal signals influenced by nonstationary external forcing). One and two-dimensional models are notably used in estuaries to represent longitudinal variations in tidal properties and to produce cotidal charts, respectively. In these models, imposed discharges are generally kept constant at the upstream boundaries, with tidal components forced at the downstream entrance, and simulations are performed for a sufficiently long period (typically 1 year) to extract tidal properties at the grid nodes using traditional HA methods [see,

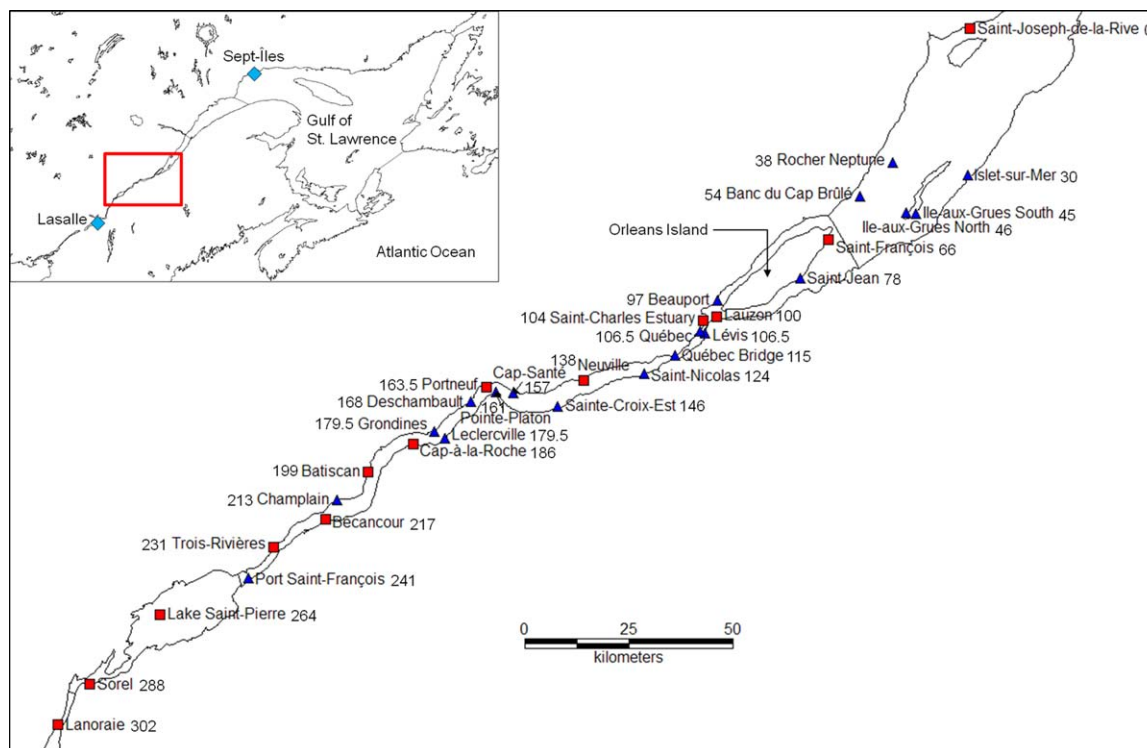


**Figure 1.** Map showing tide gauges in the St. Lawrence fluvial estuary: (red squares) analysis stations; (blue triangles) validation stations; (light blue diamonds) reference stations for ocean tidal range (Sept-Îles) and river discharge (Lasalle). River kilometers are shown beside each station name.

e.g., *El-Sabh and Murty, 1990; Parker, 1991*). Although these models provide a basis for understanding the nonlinear interactions of tides with friction and river flow, continuous functions of the response of tidal properties (i.e., amplitudes and phases of tidal constituents) to river flow and ocean tidal forcing are generally not incorporated in the analyses, thus limiting the predictive capabilities of the models.

Several methods or improvements to traditional harmonic methods have been developed to better represent transient tidal processes (for an overview, see, e.g., *Jay and Kukulka [2003]* and *Parker [2007]*). Among the latest, an adaptation of classical HA to nonstationary tides, NS\_TIDE, has been proposed and successfully applied in the Columbia River to a tidal signal strongly altered by river flow [*Matte et al., 2013*]. In NS\_TIDE, the nonstationary forcing is built directly into the HA basis functions using a functional representation derived from river-tide propagation theory [*Jay, 1991*] and adapted from *Kukulka and Jay [2003a, 2003b]* and *Jay et al. [2011]*. Tidal-fluvial interactions are decoupled, allowing stage and tidal properties to be modeled separately as a function of time, in terms of time-varying external forcing by river flow and ocean tides. Moreover, the independence of the tidal components is ensured through redefined constituent selection and error estimation procedures.

In the St. Lawrence River, tide tables are produced using HA for all ports in the gulf and estuary up to Saint-Joseph-de-la-Rive (Figure 1). Upstream of Saint-Joseph-de-la-Rive, the influence of river discharge is included in the prediction using a one-dimensional model (ONE-D) of the St. Lawrence River [*Dailey and Harleman, 1972; Morse, 1990*]. The ONE-D model solves the one-dimensional St. Venant equations. It is forced downstream with harmonic constituents at Saint-Joseph-de-la-Rive and upstream with daily discharges at the outlets of Lake Saint-Louis and Lake Des-Deux-Montagnes for a typical year, i.e., an average spring freshet followed by low flows in summer and rising flows in fall. The model is run for the entire year, and hourly water levels, along with the times and heights of high and low tides, are extracted to produce tide tables at the stations.

The model is also run in operational mode, fed by the freshwater outflows from Lake Ontario and the Ottawa River. These outflows are forecast 30 days ahead and carefully regulated to prevent flooding in the

spring and to avoid low water conditions throughout the year, for navigation safety purposes. For the first 48 h, the wind forecast of Environment Canada (Meteorological Service of Canada) for the St. Lawrence Estuary is used to calculate wind-induced storm surge at the downstream boundary. The effect of ice cover on the flow is also included in winter time, by restricting the flow on some sections [Lefaivre et al., 2009].

This operational forecast system meets the need for a water level prediction throughout the entire St. Lawrence system and has proven to be quite valuable to the Canadian Coast Guard, the Canadian Port Authorities, ship owners, and in diverse applications from coastal flooding forecasts and ice cover management to hydrodynamic and climate change impact studies [Lefaivre et al., 2009]. However, a discrepancy remains between the harmonic-based predictions made in the estuary and gulf and the hydrodynamic-based predictions made upstream, which is strongly linked to the nature of the tides in both regions. Traditional harmonic methods assume that tides at a coastal station can be represented by a sum of sine waves with constant amplitudes and phases, whose frequencies are derived from tidal potential and nonlinear shallow-water interactions. Hydrodynamic models, for their part, solve the shallow water equations for the conservation of mass and momentum. They offer a spatially integrated representation of water levels and velocities in a system at the scale of the grid element size, whereas regression models such as HA or others offer temporally integrated views of a tidal signal measured at one or a few points in space, but usually over much larger periods of time [e.g., Jay et al., 2011], typically expressed in terms of its frequency content. Consequently, the dynamical understanding that can be gained in the upstream and downstream portions of the St. Lawrence is inherently different due to drastically different methods used to represent the tides.

In this paper, a harmonic-based, nonstationary tidal propagation model of the St. Lawrence fluvial estuary is developed through application of NS\_TIDE to 13 tide gauges distributed between Saint-Joseph-de-la-Rive and Lanoraie (Figure 1). In order to represent tidal properties in a continuous manner throughout the system, model coefficients are spatially interpolated between the stations, thus yielding a spatial model of the evolution of stage and tidal properties as a function of upriver location and forcing conditions. To validate the model, water level predictions are produced at 19 intermediate (mostly temporary) stations and compared to observations as well as to forecasts made by the operational ONE-D model. The objectives of this work are (1) to develop a spatial harmonic model capable of predicting variations in stage and tidal properties as a function of nonstationary forcing variables, and (2) to improve current knowledge on tidal-fluvial processes in the St. Lawrence fluvial estuary. The goal is not to supplant the operational ONE-D forecast model, which serves its purpose of predicting water levels in the St. Lawrence River, but to complement it by exploring temporal changes in the frequency content of the tides, thereby bringing new insights into tidal-fluvial interactions. Such a treatment also guarantees continuity between predictions made in the upper and lower St. Lawrence by use of harmonic methods throughout.

## 2. Methods

### 2.1. Regression Models

Classical HA was given a structure based on a modern understanding of the tidal potential by Doodson [1921]. Following a reformulation of Doodson's work by Godin [1972], tidal heights  $h$  are typically modeled as:

$$h(t) = b_{0,0} + \sum_{k=1}^n [b_{1,k} \cos(\sigma_k t) + b_{2,k} \sin(\sigma_k t)], \tag{1}$$

where  $t$  is time,  $\sigma_k$  are a priori known frequencies,  $n$  is the number of constituents, and  $b_{0,0}$ ,  $b_{1,k}$ , and  $b_{2,k}$  are unknown coefficients determined by regression analysis to best fit the observations.

Improvements to traditional harmonic methods have been made in the recent years [e.g., Foreman et al., 2009; Leffler and Jay, 2009; Codiga, 2011]. Among those, Leffler and Jay [2009] incorporated robust statistical fitting through iteratively reweighted least-squares (IRLS) analyses [Holland and Welsch, 1977; Huber, 1996] to increase the level of confidence in computed parameters. With these inclusions, the solution to equation (1) is obtained by minimizing the sum of weighted residuals:

$$E = \sum_{j=1}^m w_j^2 (h_j - y_j)^2, \tag{2}$$

where  $y$  is the observations,  $m$  is the record length, and  $w$  is a weighting function. Setting all  $w_j$  ( $j = 1 \dots m$ ) values to 1 reduces the equation to the ordinary least-squares (OLS) solution, while introducing a weighting function allows one to penalize outliers with lower values of  $w_j$ , thus downweighting observations that increase residual variance.

A generalization of traditional HA has also been proposed by *Matte et al.* [2013] for the study of nonstationary tides, more specifically, river tides, implemented through modifications of the T\_TIDE toolbox in Matlab [*Pawlowicz et al.*, 2002]. To include contributions caused by external forcing (river flow and ocean tides) and nonlinear interactions, a functional representation, derived from a theory of river-tide propagation [*Jay*, 1991] by *Kukulka and Jay* [2003a, 2003b] and *Jay et al.* [2011], was embedded directly in the HA basis functions implemented in NS\_TIDE [*Matte et al.*, 2013]. This formulation is based on the Tschebyschev decomposition of the bed stress  $\tau_B = \rho C_D |U|U$  of the one-dimensional St. Venant equations [*Dronkers*, 1964], which is the dominant source of nonlinearities in shallow rivers; here,  $\rho$  is the water density,  $C_D$  is the drag coefficient, and  $U$  is the velocity. It is obtained for the critical convergence regime defined by *Jay* [1991], in which case tides can be considered as diffusive [*LeBlond*, 1978]. In this regime, tidal and fluvial flows are assumed to be of similar magnitude and channel convergence moderate. Conceptually, the constants  $b_{0,0}$ ,  $b_{1,k}$ , and  $b_{2,k}$  in equation (1) are replaced by functions of river flow and greater diurnal tidal range (i.e., the difference between higher high water and lower low water within a day) at a convenient station removed from fluvial influence:

$$b_{l,k}(t) = a_{0,l,k} + a_{1,l,k} Q^p(t) + a_{2,l,k} \frac{R^q(t)}{Q^r(t)}, \tag{3}$$

where  $Q$  is the river flow ( $m^3 s^{-1}$ );  $R$  is the greater diurnal tidal range (m);  $p, q, r$  are the exponents for each station and frequency band;  $a_{0,l,k}, a_{1,l,k}, a_{2,l,k}$  are the model coefficients for each station and frequency;  $k$  is the index for tidal constituents ( $k = 1, n$ );  $l$  is the index for coefficients ( $l = 0, 2$ ).

The coefficient  $a_{0,l,k}$  in equation (3) is primarily determined by the convergence or divergence of the channel cross section. The second term represents the nonlinear response of tidal parameters to river flow, approximated in theory by a two-term function [*Jay*, 1991], but reduced in equation (3) to one discharge term with its associated coefficient and exponent. Also, the variable  $Q$  appearing in equation (3) is itself a simplification of  $U = Q/A(Q)$ , where  $A(Q)$  is the cross-channel area. Variations in channel geometry and peripheral intertidal areas are thus absorbed into the model parameters. The last term in equation (3) represents the effects of frictional interaction due to neap-spring variability, responsible for the tidal monthly changes in MWL and tidal properties. In practice, deviations from theory, due to time-varying channel geometries and variations in the ratio of river flow to tidal currents as a function of upriver distance, can be accounted for by tuning the exponents by station [e.g., *Jay et al.*, 2011].

In the following application, exponents are set to the theoretical values of *Kukulka and Jay* [2003a, 2003b], rather than iteratively optimized, to allow comparisons between stations and development of a spatial model (see next section). Also, at each station, a time lag is applied to the forcing variables  $Q$  and  $R$ , representing the average time of propagation of the waves to the station. The  $Q$  and  $R$  time series are lagged by calculating the maximum correlation between  $Q$  or  $R$  and the observations  $y$  (either low-passed or range-filtered). More complex lag functions could be used to better capture the varying propagation times as a function of river stage and improve synchronism between the input time series, although they are not applied here. The final form of the model, with the exponents replaced by their theoretical values, is obtained by distributing equation (3) into equation (1):

$$h(t) = \underbrace{c_0 + c_1 Q^{2/3}(t - \tau_Q) + c_2 \frac{R^2(t - \tau_R)}{Q^{4/3}(t - \tau_Q)}}_{\text{stage model or } s(t)} + \sum_{k=1}^n \underbrace{\left[ \left( d_{0,k}^{(c)} + d_{1,k}^{(c)} Q(t - \tau_Q) + d_{2,k}^{(c)} \frac{R^2(t - \tau_R)}{Q^{1/2}(t - \tau_Q)} \right) \cos(\sigma_k t) + \left( d_{0,k}^{(s)} + d_{1,k}^{(s)} Q(t - \tau_Q) + d_{2,k}^{(s)} \frac{R^2(t - \tau_R)}{Q^{1/2}(t - \tau_Q)} \right) \sin(\sigma_k t) \right]}_{\text{tidal-fluvial model or } f(t)}, \tag{4}$$

where  $s$  and  $f$  denote the stage and tidal-fluvial models, respectively; the superscripts (c) and (s) refer to the cosine and sine terms, respectively;  $c_i$  ( $i = 0, 2$ ) are the model parameters for the stage model;  $d_{i,k}$  ( $i = 0, 2$ ) are the model parameters for the tidal-fluvial model;  $\tau_Q$  and  $\tau_R$  are the time lags applied to the  $Q$  and  $R$  time

series, respectively. The regression coefficients ( $c_0$ ,  $c_1$ ,  $c_2$ ,  $d_{0,k}$ ,  $d_{1,k}$ , and  $d_{2,k}$ ) in equation (4) are determined by application of equation (2).

Each tidal component of the tidal-fluvial model can be represented in the form of a time series:

$$Z_k(t) = z_k(t)e^{i\sigma_k t} + z_{-k}(t)e^{-i\sigma_k t} = |z_k(t)|e^{-i\phi_k(t)}e^{i\sigma_k t} + |z_{-k}(t)|e^{i\phi_k(t)}e^{-i\sigma_k t}, \quad (5)$$

with time-dependent amplitudes and phases respectively given by:

$$|Z_k(t)| = |z_k(t)| + |z_{-k}(t)| \quad (6a)$$

and

$$\phi_k(t) = \arctan [\text{Im}(z_{-k}(t))/\text{Re}(z_{-k}(t))]. \quad (6b)$$

In terms of the coefficients in equation (4),  $z_{-k}(t)$  can be rewritten as:

$$z_{-k}(t) = z_k^*(t) = \frac{1}{2}(A_k \cos \alpha_k + B_k \cos \beta_k + C_k \cos \gamma_k) + i \frac{1}{2}(A_k \sin \alpha_k + B_k \sin \beta_k + C_k \sin \gamma_k), \quad (7)$$

where the amplitudes  $A_k$ ,  $B_k$ , and  $C_k$ , and phases  $\alpha_k$ ,  $\beta_k$ , and  $\gamma_k$  are defined as:

$$A_k = \sqrt{(d_{0,k}^{(c)})^2 + (d_{0,k}^{(s)})^2}, \quad (8a)$$

$$B_k = Q(t - \tau_Q) \sqrt{(d_{1,k}^{(c)})^2 + (d_{1,k}^{(s)})^2}, \quad (8b)$$

$$C_k = \frac{R^2(t - \tau_R)}{Q^{1/2}(t - \tau_Q)} \sqrt{(d_{2,k}^{(c)})^2 + (d_{2,k}^{(s)})^2}, \quad (8c)$$

$$\alpha_k = \arctan (d_{0,k}^{(s)}/d_{0,k}^{(c)}), \quad (9a)$$

$$\beta_k = \arctan (d_{1,k}^{(s)}/d_{1,k}^{(c)}), \quad (9b)$$

$$\gamma_k = \arctan (d_{2,k}^{(s)}/d_{2,k}^{(c)}). \quad (9c)$$

Hence, time series of MWL and tidal amplitudes and phases for each resolved frequency can be generated for any given forcing time series  $Q$  and  $R$ .

## 2.2. Spatial Model

Using the regression models described in the previous section, stage and tidal properties were determined at a finite number of stations located along the St. Lawrence. A spatial model is required to represent these properties in a continuous manner so that spatial interpretation of the physics becomes possible as well as predictions at arbitrary locations. The criteria used in the selection of interpolating functions were the smoothness properties and degree of approximation. Here interpolation of the coefficients in equation (4) is made between the stations using piecewise cubic Hermite interpolants [Fritsch and Carlson, 1980]. Cubic Hermite functions are exact interpolants. They are continuous up to the first derivatives only and do not generate extrema or oscillations. Furthermore, slopes between stations are determined in a way that the shape of the data (e.g., local extrema, convexity) is preserved and monotonicity is respected.

Spatial interpolation of tidal harmonic fields is more robust and accurate when performed in complex amplitude form, in this case using model coefficients, rather than interpolating amplitudes and phases directly. Large errors can otherwise be introduced; for example, the average of  $350^\circ$  and  $10^\circ$  is  $0^\circ$ , not  $180^\circ$  if inappropriately interpolated [Martin et al., 2009; Park et al., 2012]. Hence, model coefficients in equation (4) were spatially interpolated, so that they become a function of the distance  $x$ , i.e.,  $c_i \Rightarrow c_i(x)$  and  $d_{i,k} \Rightarrow d_{i,k}(x)$ . For the interpolation to be relevant, the analysis parameters (i.e., model exponents, tidal constituents, record length and analysis period, etc.) must be the same at all stations. They are detailed in the next section.

## 3. Application to the St. Lawrence Fluvial Estuary

### 3.1. Setting

The St. Lawrence River connects the Atlantic Ocean with the Great Lakes (Figure 1). It is the third largest river in North America, with a catchment area of  $\sim 1.6 \times 10^6 \text{ km}^2$  and an average freshwater discharge of

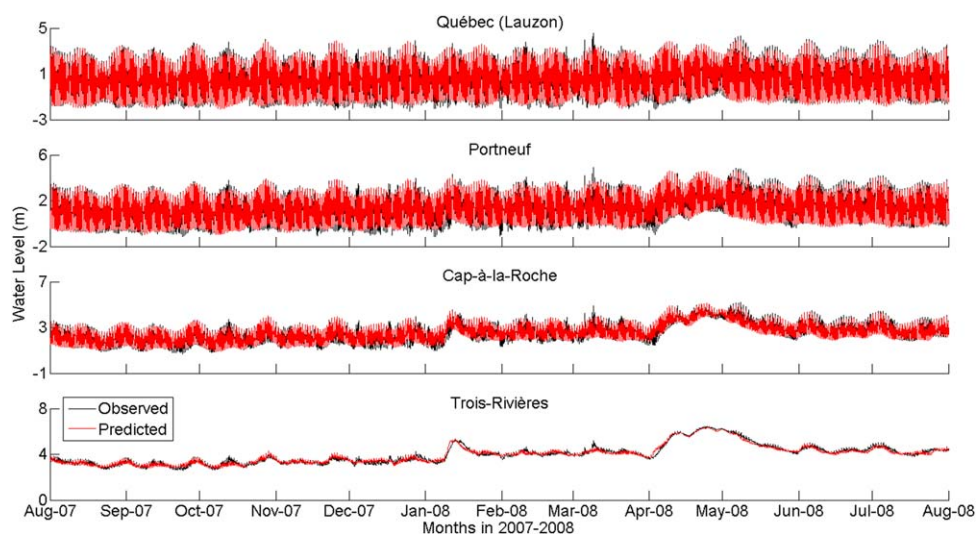


**Figure 2.** (black) Observed water levels at Québec (Lauzon), Portneuf, Cap-à-la-Roche, and Trois-Rivières from August 2007 to August 2008. (red) Water level hindcast from NS\_TIDE.

$12,200 \text{ m}^3 \text{ s}^{-1}$  at Québec. Minimum and maximum daily net discharges in the St. Lawrence respectively amounted to  $7000$  and  $32,700 \text{ m}^3 \text{ s}^{-1}$  at Québec over the 1960–2010 period, taking into account the contribution of all tributaries [Bouchard and Morin, 2000]. The effects of such variations on MWL and tidal range are severe, particularly in the upper portion of the St. Lawrence fluvial estuary above Deschambault [Godin, 1999].

Ocean tides are amplified as they enter the St. Lawrence until they reach their maximum amplitude in the upper estuary at Saint-Joseph-de-la-Rive (hereafter defined as river kilometer (rkm) 0) with a 7 m range during the largest spring tides. They are then damped on their way upstream due to frictional effects. Tides are mixed diurnal, semidiurnal, with ratios of major semidiurnal to diurnal amplitudes, i.e.,  $(|M_2| + |S_2|)/(|K_1| + |O_1|)$ , around 5:1 at Saint-Joseph-de-la-Rive and decreasing upstream, the diurnal components being damped less rapidly than the semidiurnals.

The St. Lawrence fluvial estuary spans 180 rkm from the eastern tip of Orleans Island, located at the upper limit of saline intrusion, to the eastern end of Lake Saint-Pierre (Figure 1). While tides can be considered as stationary in the estuary and gulf, they are highly nonlinear and nonstationary in the fluvial estuary. Godin [1999] suggested separation of the fluvial estuary into three zones: (1) Québec–Portneuf (rkm 100–163.5), (2) Portneuf–Cap-à-la-Roche (rkm 163.5–186), and (3) Cap-à-la-Roche–Trois-Rivières (rkm 186–231). Observed water levels at these stations are presented in Figure 2 for a 1 year period characterized by both very low and very high flows (see Figure 3). In the first zone (Québec–Portneuf), tidal ranges vary between approximately 3 and 6 m depending on the station and phase of the neap-spring cycle. Increases in water levels of more than  $1 \text{ m h}^{-1}$  occur during the rising tide, leading to rapid changes in flow conditions as well as in the surfaces of wetted areas. This generates strong current reversals with daily peak tidal discharges being up to 5 times greater than the daily average in both upstream and downstream directions. The second zone (Portneuf–Cap-à-la-Roche) marks the transition between the tidal and tidal-fluvial regime. It is characterized by a sharp increase in bed slope at the Richelieu Rapid near Deschambault (rkm 168). The tidal signal is strongly distorted and progressively damped as a result of friction and river discharge. Ebb tides are lengthened and flood tides are steepened and shortened, part of the energy from the primary tidal constituents being nonlinearly transferred to their superharmonics. The limit where the flow becomes unidirectional (i.e., only one slack water) moves between Grondines (rkm 179.5) and Becancour (rkm 217) as a function of tidal range and river flow, near the limit between zones 2 and 3. In the third zone (Cap-à-la-Roche–Trois-Rivières), water level variations are dominated by the river flow cycle. At Trois-Rivières (rkm 231), the fortnightly modulation of MWL induced by the neap-spring cycle exceeds in amplitude the semidiurnal tide [LeBlond, 1979], whose range is 0.2 m for a mean tide. Leaving the tidal river per se, most of the

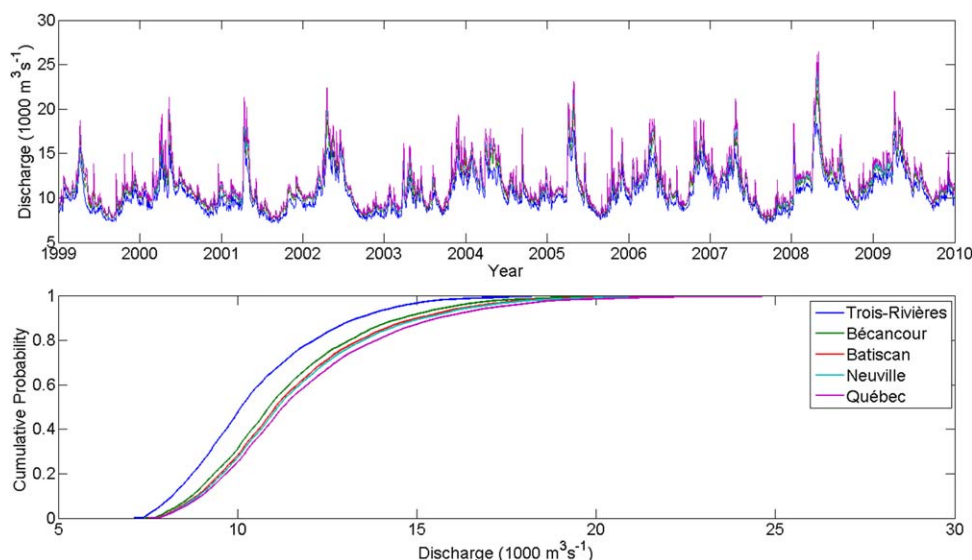


**Figure 3.** Forcing discharges in the St. Lawrence River for the 1999–2009 period: (top) discharge time series at Trois-Rivières, Bécancour, Batiscan, Neuville, and Québec; (bottom) empirical cumulative distribution function.

short-period tide (i.e., diurnal, semidiurnal, etc.) is damped in Lake Saint-Pierre (rkm 264), but long-period oscillations are still noticeable as far as Montreal (rkm 360).

### 3.2. Analysis Parameters

NS\_TIDE was applied to hourly water level data at 13 tide gauges, maintained by Canada’s Department of Fisheries and Oceans (DFO), distributed between Saint-Joseph-de-la-Rive and Lanoraie (Figure 1); they are listed in Table 1. Time series composed of more than 90,000 good data points were selected for the analysis, for a reference period extending from 1999 to 2009 inclusively, the remaining 19 stations being used for validation (Table 2). Validation stations are a mix of temporary DFO’s tide gauges and pressure sensors installed from May to October 2009 (Figure 1) [Matte et al., 2014]. The 11 year analysis period was chosen for its wide range in river flow. Also, no major construction or dredging work was done after 1998 [Côté and Morin, 2007], so that stage and tidal properties are expected to be rather stable during that time period. Moreover, the proportion of fine materials is about 20% in the St. Lawrence, between Sorel and Orleans Island, with an average sedimentation rate of 4 mm yr<sup>-1</sup> [Couillard, 1987]. Most of the silting-up is dredged for maintenance of the navigational channel or flushed in fall and spring [Gagnon, 1995; Robitaille, 1998b, 1998a] and thus has a limited effect on tidal propagation.

Five daily discharge time series  $Q$  were used as forcing conditions, each of which is an estimate based upon continuous water level measurements at the station of Lasalle (Figure 1) and has been modified to account

**Table 1.** Parameters of the NS\_TIDE Analyses at the Tide Gauges for the 1999–2009 Period, Including the Number of Good Data Points, and Their Corresponding Discharge Time Series and Time Lags

rkm	Station	Good Data	Q Time Series	$\tau_Q$ (h)	$\tau_R$ (h)
0	Saint-Joseph-de-la-Rive	93,149	Québec	-14	5
66	Saint-François	95,418	Québec	-14	5
100	Lauzon	95,048	Québec	-14	5
104	Saint-Charles River	94,608	Québec	-14	5
138	Neuville	95,449	Neuville	-6	6
163.5	Portneuf	94,833	Neuville	-6	6
186	Cap-à-la-Roche	95,301	Batiscan	16	7
199	Batiscan	93,062	Batiscan	16	7
217	Bécancour	95,649	Bécancour	26	9
231	Trois-Rivières	95,583	Bécancour	26	9
264	Lake Saint-Pierre	90,395	Bécancour	26	9
288	Sorel	95,718	Trois-Rivières	28	10
302	Lanoraie	96,119	Trois-Rivières	28	10

**Table 2.** Validation Stations From DFO and Pressure Sensors, Along With Their Corresponding Discharge Time Series, Record Lengths and Number of Good Data Points for the 1999–2009 Period<sup>a</sup>

rkm	Station	Source	Record Length (yr)	Good Data	Q Time Series
30	<i>Islet-sur-Mer</i>	<i>Pressure sensor</i>	0.4	13,522	<i>Quebec</i>
38	Rocher Neptune	DFO	4.4	19,433	Quebec
45	<i>Ile-aux-Grues South</i>	<i>Pressure sensor</i>	0.3	9,780	<i>Quebec</i>
46	<i>Ile-aux-Grues North</i>	<i>Pressure sensor</i>	0.3	9,785	<i>Quebec</i>
54	Banc du Cap Brûlé	DFO	3.1	12,436	Quebec
78	Saint-Jean	DFO	3.5	16,988	Quebec
97	<i>Beauport</i>	<i>Pressure sensor</i>	0.4	13,410	<i>Quebec</i>
106.5	Lévis	Pressure sensor	0.4	13,415	Quebec
106.5	Quebec	Pressure sensor	0.4	12,769	Quebec
115	Quebec Bridge	Pressure sensor	0.4	13,617	Quebec
124	Saint-Nicolas	Pressure sensor	0.4	12,963	Quebec
146	Sainte-Croix-Est	Pressure sensor	0.4	13,052	Neuville
157	Cap-Santé	Pressure sensor	0.4	12,765	Neuville
161	Pointe-Platon	Pressure sensor	0.4	12,964	Neuville
168	Deschambault	Pressure sensor	0.4	11,243	Batiscan
179.5	Leclercville	Pressure sensor	0.4	11,966	Batiscan
179.5	Grondines	Pressure sensor	0.4	12,431	Batiscan
213	Champlain	Pressure sensor	0.4	11,452	Bécancour
241	Port Saint-François	DFO	10.3	63,857	Bécancour

<sup>a</sup>Pressure sensor data are sampled at a 15 min interval, while DFO's data are hourly. Stations in italics are not covered by the main branch of the ONE-D model.

for flows from tributaries. The data were produced based on a stage-discharge relation at Lasalle. Fort-nightly variations of MWL due to low-frequency tides were considered as part of the noise. The flows from tributaries were reconstructed by adding the discharge measured at an upstream station to the estimated lateral inflow, consisting of surface water runoff and groundwater inflow. Virtually no data are available for groundwater inflow, so that only surface water runoff was considered, based on gauged areas. For ungauged areas, the inflow was estimated from the runoff coefficient of an adjoining gauged area. Relations for each tributary to the St. Lawrence were developed by Morse [1990] and adapted by Bouchard and Morin [2000]. Since the drainage area in the St. Lawrence increases moving downstream, the contribution of tributaries was progressively added to the total discharge time series used at the stations. The reconstructed discharge time series used in the analyses are presented in Figure 3 and listed in Table 1 for each station. Discharge time series used at the validation stations are shown in Table 2. Differences in discharge between Trois-Rivières and Quebec for the 1999–2009 period reached a maximum of  $8700 \text{ m}^3 \text{ s}^{-1}$  in April 2008 during the freshet (Figure 3). Minimum and maximum discharges at Quebec for that period were observed in September 2007 ( $7600 \text{ m}^3 \text{ s}^{-1}$ ) and April 2008 ( $26,400 \text{ m}^3 \text{ s}^{-1}$ ), respectively, which are fairly extreme when compared to the most extreme flows that occurred in March 1965 ( $7000 \text{ m}^3 \text{ s}^{-1}$ ) and April 1976 ( $32,700 \text{ m}^3 \text{ s}^{-1}$ ) for the 1960–2009 period. Empirical cumulative distribution functions are shown in Figure 3 for each discharge time series and were used to define quantiles of river flow (see next section).

Sept-Îles was chosen as the reference station for ocean tidal forcing (Figure 1), similarly to Godin's [1999] regression model, because it is removed from fluvial influence and sufficient data are available. Greater diurnal tidal ranges  $R$  were extracted from hourly data at Sept-Îles. Water levels were high-pass filtered, then re-interpolated using (exact) cubic spline functions to a 6 min interval in order to capture the tidal extrema (data are smooth and regularly sampled so that no oscillations are generated during interpolation). Tidal ranges were calculated as the difference between higher high water and lower low water using a 27 h moving window with 1 h steps, then smoothed to eliminate discontinuities, similarly to Kukulka and Jay's [2003a] tidal range filter. The time series of tidal range for the analysis period is presented in Figure 4, along with its corresponding empirical cumulative distribution function, used to define quantiles of tidal range.

Time lags  $\tau_Q$  and  $\tau_R$  for both  $Q$  and  $R$  time series are presented in Table 1. They were set to identical values for stations sharing the same discharge time series, corresponding to the average lags for the stations concerned. For predictions made at arbitrary locations, e.g., at the validation stations, the same lags as the ones used at neighbouring stations were applied to the time series. It is noteworthy that for the Trois-Rivières station, the discharge time series for Bécancour was used instead of that of Trois-Rivières, in order to include

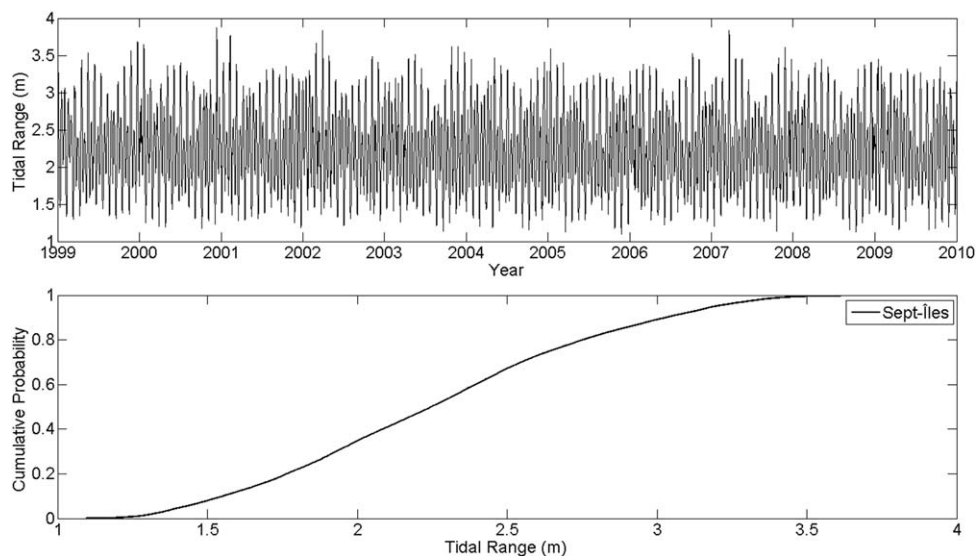


**Figure 4.** Forcing tidal range in the St. Lawrence River for the 1999–2009 period: (top) tidal range time series at Sept-Îles; (bottom) empirical cumulative distribution function.

the backwater effects from the Saint-Maurice River, located 1 km downstream of the station. This effect propagates up to the station of Lake Saint-Pierre.

In the development of a spatial model, identical analysis parameters must be applied to each station to ensure that spatial variations in the coefficients are not the result of changes in model properties, but that they are attributable to tidal-fluvial processes. Preliminary tests on the model exponents in equation (3) showed that model performance was little sensitive to their value, as deviations from theoretical exponents were compensated by changes in the regression coefficients. Similar conclusions were drawn from the sensitivity analysis performed by *Matte et al.* [2013]. Therefore, model exponents were set to the theoretical values used by *Kukulka and Jay* [2003a, 2003b], as they appear in equation (4). The same tidal constituents were imposed at all stations to allow interpolation of model coefficients throughout the system. As a consequence, errors for some constituents may grow upstream, while some other constituents become less significant downstream. The IRLS analyses (cf. equation (2)) were performed using a Cauchy weighting function with a default tuning constant of 2.385 [*Leffler and Jay*, 2009; MathWorks, R2010a MathWorks documentation, <http://www.mathworks.com/help/releases/R2010a/helpdesk.html>].

The allowed frequency separation in NS\_TIDE is dictated by a redefined Rayleigh criterion, which takes into account the overlap between frequencies associated with their tidal cusps [*Munk et al.*, 1965]. The width of these cusps reflects the intensity of modulation of the tidal components. Therefore, the inclusion of too many constituents with overlapping cusps can lead to erroneous estimates of tidal properties [e.g., *Godin*, 1999]. One typical symptom of an overdetermined solution (i.e., too many constituents) is that closely spaced components take very large (unreal) amplitudes, their phases are almost  $180^\circ$  out of phase, so they cancel partially, and phase errors are very large (typically exceeding  $100^\circ$ ). Conversely, not resolving enough constituents may result in oscillation of the tidal amplitudes as a compensation for modulations that would normally occur between pairs of constituents not included in the analyses. In the most extreme case, only including one component per tidal band would yield similar results as continuous wavelet transform (CWT) [*Flinchem and Jay*, 2000]. Here tidal constituents were selected, partly based on rather permissive constituent selection criteria ( $\eta = 0.5$  and mean signal-to-noise ratio (SNR)  $\geq 2$ ; see *Matte et al.* [2013] for a definition of the parameters). Constituent amplitudes and phases were then carefully inspected to detect artifacts arising from the method. To ensure that included constituents have a physical meaning, comparisons of time-averaged tidal properties (especially the phases) with those given by standard HA were made, assuming that HA accurately represents the average frequency content of the time series. Constituents presenting nonphysical characteristics were excluded from the analyses, while some others were progressively added to reduce oscillations in the tidal amplitudes of principal components. In the end, the tidal-fluvial model

**Table 3.** Tidal Constituents Included in the Analyses, for Each Tidal Band From Diurnal to Eight-Diurnal (D1–D8)

Tidal Bands	Constituents
D <sub>1</sub>	$\sigma_1, Q_1, \rho_1, O_1, P_1, K_1, \theta_1, J_1, OO_1$
D <sub>2</sub>	$\varepsilon_1, 2N_2, \mu_2, N_2, \nu_2, M_2, \lambda_2, L_2, S_2, K_2, MSN_2$
D <sub>3</sub>	$MO_3, SO_3, MK_3$
D <sub>4</sub>	$MN_4, M_4, SN_4, MS_4, MK_4, S_4, SK_4$
D <sub>5</sub>	$2MK_5$
D <sub>6</sub>	$2MN_6, M_6, 2MS_6, 2MK_6, 2SM_6, MSK_6$
D <sub>7</sub>	$3MK_7$
D <sub>8</sub>	$M_8$

was forced using the same 39 components at all stations, listed in Table 3. At Saint-Joseph-de-la-Rive (rkm 0), these 39 constituents explain 98% of the variance in water levels, with classical HA. Low-frequency variations in water levels, for their part, are represented by the stage model (cf. equation (4)), rather than the usual low-frequency harmonic constituents.

The time reference for the analyses was Eastern Standard Time. Greenwich phases were computed, with no nodal corrections. The latter are performed in NS\_TIDE in the same manner as T\_TIDE [Pawlowicz *et al.*, 2002]

and should be applied on overlapping 366 day periods. However, for the coefficients of the nonstationary analysis to be robust, a record length that covers the widest dynamic range of flow conditions is sought. The chosen 11 year period met this criterion. NS\_TIDE does not currently embed the nodal corrections in the least squares matrix, which would remove the need for assumptions that underlie usual postfit corrections and that may restrict the length of the analysis period [Foreman *et al.*, 2009]. Nevertheless, modulations of the main tidal constituents by their satellites are small in rivers relative to the effects of stage variations. Nodal modulations are also modified by fluvial modulations. In fact, deviations from the equilibrium constants may occur due to friction and shallow-water effects, which may lead to systematic errors in the estimation of tidal constituents [Amin, 1983, 1985, 1993; Shaw and Tsimplis, 2010]. In practice, it is virtually impossible to separate the modulation effects on the main tidal constituents by river flow and tidal range from those stemming from changes in lunar declination (see, e.g., Matte *et al.* [2013] for further discussion). For these reasons, nodal corrections were not included in the analyses.

To assess model performance, water level hindcasts were compared to results from classical HA at the stations. Standard HA [Pawlowicz *et al.*, 2002; Leffler and Jay, 2009] were performed using a threshold SNR of 2 for constituent rejection. The number of replicates for the error estimation was set to 300 and a correlated noise model was used. The same weighting function and tuning constant as for the nonstationary analyses were used. To further validate model predicting capabilities, water level forecasts were produced at all stations for a period free of ice extending from 21 May to 21 October 2009, during which pressure sensors were in place. Results were compared to simulations from the ONE-D model of the St. Lawrence without considering the effects of wind. The numerical scheme and formulation of the model are detailed in Hicks [1997], along with a thorough analysis of its performance.

### 3.3. Results

#### 3.3.1. Model Performance

Figure 2 shows water level hindcasts from NS\_TIDE compared to observations at four selected stations for the 2007–2008 period, characterized by very low and very high flows (cf. Figure 3). Predicted signals follow the variations in tidal amplitude and in MWL with good accuracy at both upstream and downstream stations.

Statistics obtained from classical HA and NS\_TIDE at the analysis stations of Table 1 for the 1999–2009 period are presented in Figure 5. They include the number of model coefficients solved for (different from  $n$ , the number of tidal constituents; see equation (4)), the residual variance, root-mean-square errors (RMSE), and maximum absolute errors. The only criteria for constituent selection and rejection in HA are based on the record length and error level in coefficients, respectively. As shown in Figure 5a, the total number of model coefficients is higher with NS\_TIDE, with nearly half the constituents of HA, due to the higher number of terms composing the nonstationary model. The ability of classical HA to explain the signal variance is comparable to NS\_TIDE at downstream stations, from Saint-Joseph-de-la-Rive (rkm 0) to Portneuf (rkm 163.5), landward of which the residual variance drastically increases for HA (Figure 5b). This coincides with the presence of rapids near Deschambault (rkm 168) combined with a rapid increase of the bottom slope, marking the transition from tidal to tidal-fluvial regimes where the influence of discharge becomes prominent.

In Figure 5c, RMSE from both methods are plotted at the stations. The curves coincide in the first 100 rkm, but the RMSE associated with NS\_TIDE sharply decrease upstream, while those of HA increase. On average,

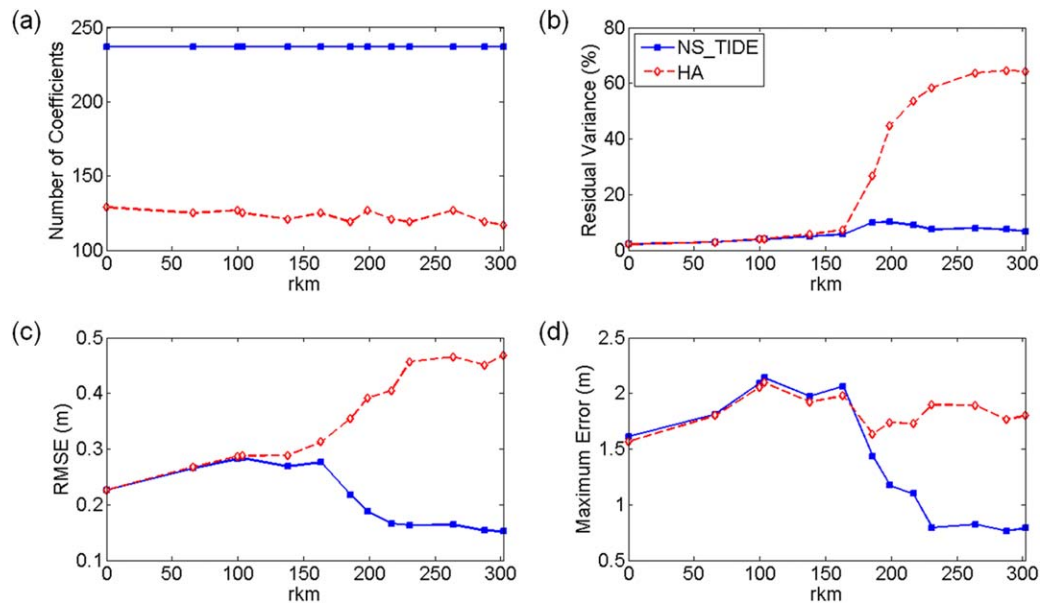


**Figure 5.** Statistics on water level hindcasts from NS\_TIDE and classical HA at the analysis stations of Table 1 for the 1999–2009 period: (a) number of model coefficients solved for; (b) residual variance; (c) root-mean-square errors (RMSE); (d) maximum absolute errors. RMSE and maximum errors are absolute values, thus decreasing with tidal range.

the NS\_TIDE analyses are far more representative of the tidal-fluvial dynamics than HA in upstream reaches of tidal rivers. At downstream stations, where the tidal signals are much more stationary (see Figure 2), NS\_TIDE is comparable to HA, thus demonstrating the validity of the model under these conditions too.

Maximum absolute errors shown in Figure 5d are again comparable between the two methods up to Portneuf (rkm 163.5), where they split. They then show a significant decrease with NS\_TIDE, attributable to a better representation of the physics by the nonstationary model. Note that both RMSE and maximum errors are absolute values; their sharp decrease past Portneuf thus also follows the decrease in tidal range.

### 3.3.2. Spatial Interpolations

The model coefficients in equation (4) were spatially interpolated using Hermite polynomials so that tidal properties may be retrieved at any points in space. Figures 6a and 6b show an example of interpolated coefficients for the stage model and the  $M_2$  component of the tidal-fluvial model, respectively. For clarity, second and third coefficients were multiplied by the average discharge and tidal range for the 1999–2009 period, as shown in the legends. In the stage model (Figure 6a), the coefficient  $c_0$  is primarily determined by river geometry. In the first  $\sim 160$  rkm, its contribution to the MWL is partly balanced by the discharge term  $c_1$ . From Portneuf (rkm 163.5) and upstream, the  $c_0$  term increases following the rapid rising of the bed slope. This may be due to a long-term water level setup caused by river-tide interaction that steepens the water surface profile [e.g., Sassi and Hoitink, 2013]. The discharge coefficient  $c_1$  increases from downstream to upstream; its effect is more pronounced past Portneuf, where changes in the tidal-fluvial regime occur. The range term  $c_2$  is responsible for fortnightly variations in MWL. The value of  $c_2$  increases gradually up to Cap-à-la-Roche (rkm 186), where the amplitude of the fortnightly wave reaches a maximum; it then decreases upstream. This tendency is consistent with the variations in  $M_f$ ,  $MS_f$ , and  $M_m$  amplitudes (not shown) calculated from classical HA at the stations.

In Figure 6b, the coefficients of the  $M_2$  component of the tidal-fluvial model are presented, where the blue curves represent the cosine part of equation (4) and the red curves represent the sine part. Both sine and cosine parts of the constant term  $d_0$  (solid lines), representing the astronomical tide, are strongly damped moving upstream. The discharge terms  $d_1$  (dashed lines) are in general opposite in sign with  $d_0$ , each pair of curves of a given part (cosine or sine) intercepting around zero, so that they cancel each other once they are summed. In other words, the sign difference between  $d_1$  and  $d_0$  means that an increase in discharge is reflected as a decrease in tidal amplitude. The range terms  $d_2$  are not consistently opposed in sign with  $d_0$ ,

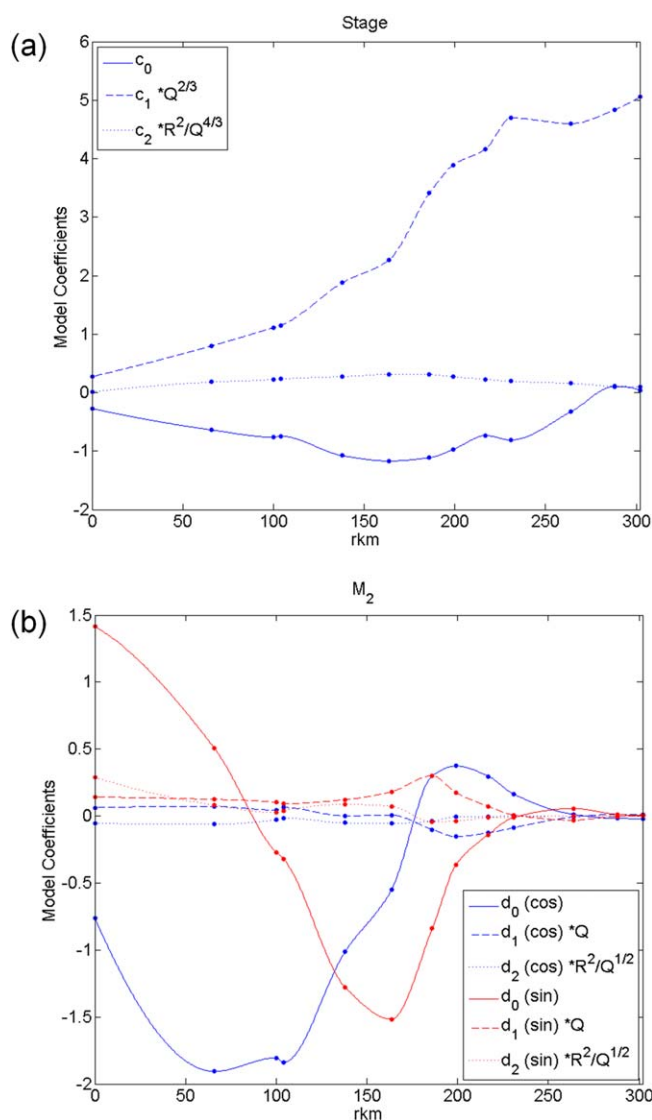


**Figure 6.** Spatially interpolated coefficients of the (a) stage model and (b)  $M_2$  component from the tidal-fluvial model. Second and third coefficients in Figures 6a and 6b were multiplied by their average discharge and tidal range for the 1999–2009 period.

so that their effect on  $M_2$  amplitudes varies along the river. The amplitudes and phases can be retrieved for each term from equations (8) and (9) for further analysis (see next sections).

### 3.3.3. Validation

To validate the model, water level predictions were generated at all 32 stations from Tables 1 and 2 and compared with observations, for the period extending from 21 May to 21 October 2009. The same exercise was done for the ONE-D model for comparison purposes. Results are presented in Figure 7. Stations identified with asterisks are not covered by the main branch of the ONE-D model and should be interpreted with caution; they are either located on the south shore of the upper estuary (downstream of Orleans Island) or in the north arm of Orleans Island. In general, residual variances, RMSE and maximum errors are lower with the ONE-D model than with NS\_TIDE, with the exception of a few upstream stations. This is not a surprising result since ONE-D has many more degrees of freedom than NS\_TIDE. The ONE-D model of the St. Lawrence is composed of 1241 sections, each described in terms of geometry and friction. It solves the one-dimensional St. Venant equations at every time step of the validation period. In comparison, the NS\_TIDE model is based on an analytical solution of the St. Venant equations for the critical convergence regime [Jay, 1991]. It is

composed of 237 parameters per station or, equivalently, 237 Hermite polynomial functions for the spatial model which are invariant in time (i.e., no need for time integration). Although much simpler, the NS\_TIDE model is capable of good accuracy, with RMSE lower than 0.3 m at all stations. This is quite low considering that tidal ranges often exceed 5 m in the downstream portion of the river. Furthermore, error at the validation stations is not systematically higher than at the analysis stations, which is an indication that the station network is dense enough to allow accurate interpolation. It also shows that the interpolation functions are well adapted to the variations in modeled parameters, and thereby to the physics of the river. Interpolation errors are discussed in section 4. Higher residual variances were obtained at the station of Champlain (rkm 213) due to a higher noise level in the observed data (Figure 7a).

To better characterize the model predicting capabilities, RMSE values were computed separately on MWL, tidal range, and height and time of high water (HW) and low water (LW). Results are shown in Figure 8. MWL are better reproduced by the ONE-D model at most stations except a few where the two models are comparable. With NS\_TIDE, the highest errors in MWL occur between Neuville (rkm 138) and Portneuf (rkm 163.5), possibly due to lateral gradients in water levels associated with channel

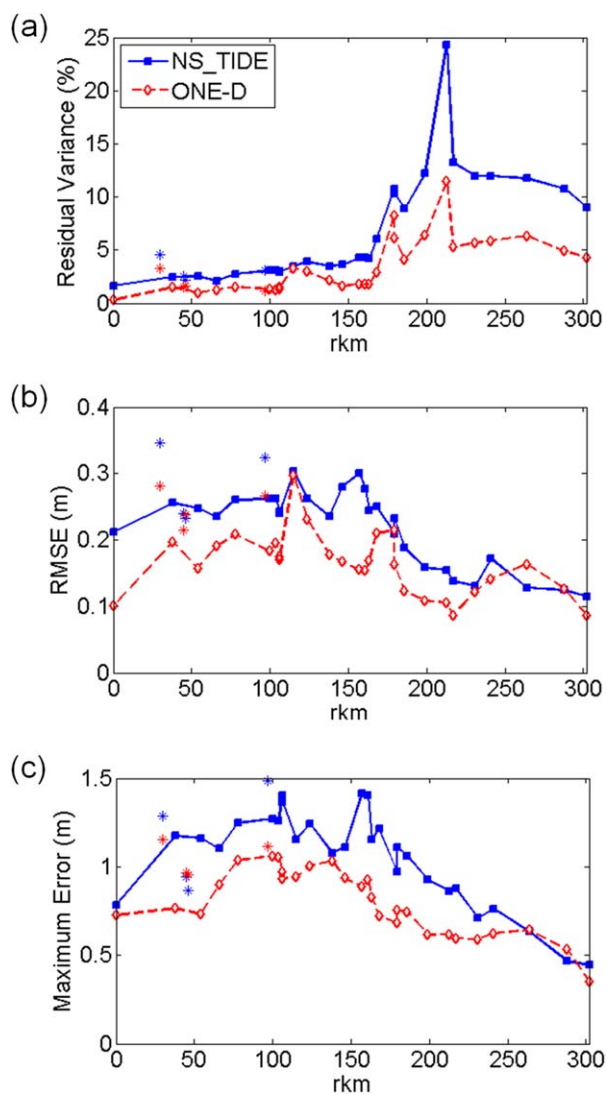


**Figure 7.** Statistics on water level predictions from NS\_TIDE and ONE-D at the stations of Tables 1 and 2 for the period from 21 May to 21 October 2009. Stations identified with asterisks are not covered by the main branch of the ONE-D model.

tide completely vanishes during high discharge events. Here the comparison of the times of occurrence of HW and LW is an indirect evaluation of tidal asymmetry.

### 3.3.4. Tidal-Fluvial Processes

To demonstrate the ability of the model to improve current knowledge on tidal-fluvial processes, results in the St. Lawrence fluvial estuary are presented in Figures 9–12. Because the objective is not to present a thorough analysis of the dynamical processes in play, results are restricted to the stage model and to five major constituents from the diurnal, semidiurnal, and quarter-diurnal bands of the tidal-fluvial model.

The harmonic representation of low frequencies in traditional HA, composed of semimonthly (Mf, MSf), monthly (Mm, MSm), semiannual (Ssa), and annual (Sa) constituents, is unable to adequately represent low-frequency river motions dominated by nonlinear interactions of tides with river flow [Parker, 2007]. In contrast, these interactions are well accounted for in NS\_TIDE because river flow and ocean tidal range are included directly in the basis functions. Longitudinal profiles of MWL are shown in Figure 9 for the 0.1, 0.5, and 0.9 quantiles of discharge and tidal range. The water surface slopes clearly exhibit three contrasting zones in the fluvial estuary, as suggested by Godin [1999], with marked changes in the slopes around

curvature. Errors in tidal range decrease with upriver distance as tidal amplitudes are damped. They reach a maximum between Quebec Bridge (rkm 115) and Saint-Nicolas (rkm 124), which can be explained by very large water depths between Lauzon (rkm 100) and Saint-Nicolas, varying approximately from 30 to 60 m. The tidal wave propagates faster with increased water depth and is less rapidly damped by bottom friction. Because the interpolation is made between Saint-Charles River estuary (rkm 104) and Neuville (rkm 138) assuming smooth variations in tidal properties, the resulting tidal ranges at intermediate stations are less accurate. This is confirmed by errors in LW heights, which are significantly higher at Quebec Bridge and Saint-Nicolas, as LW are the most sensitive to depth variations. It is however a little surprising to observe the same behaviour with ONE-D considering that water depths are taken into account in the model; this might be related to a lack of stations for calibration between Lauzon and Neuville. Furthermore, errors in the heights and times of HW are rather stable downstream of Trois-Rivières (rkm 231), while errors in the times of occurrence of LW gradually increase from downstream to upstream. They reach values of about 2 h at Trois-Rivières. LW are more sensitive to friction and river flow than HW [e.g., Godin, 1999], thus explaining the higher and increasing errors in the timing of LW. Timing errors of HW and LW upstream of Trois-Rivières were excluded, because

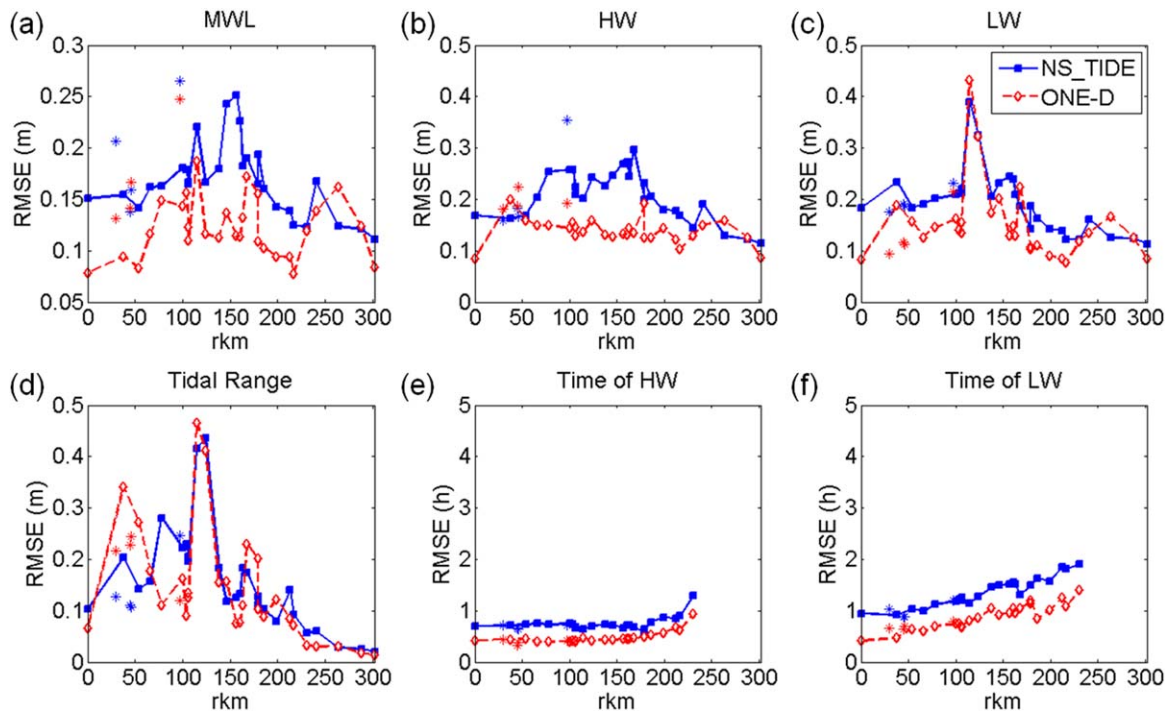


**Figure 8.** Root-mean-square error (RMSE) on predicted mean water level (MWL), tidal range, and height and time of high water (HW) and low water (LW) from NS\_TIDE and ONE-D at the stations of Tables 1 and 2 for the period from 21 May 2009 to 21 October 2009. Stations identified with asterisks are not covered by the main branch of the ONE-D model.

Portneuf (rkm 163.5) and Cap-à-la-Roche (rkm 186). The region delimited by these two stations forms a transition zone from the tidal to the tidal-fluvial regime, characterized by a rapid increase in bottom slope at the Richelieu Rapid near Deschambault (rkm 168). This supports the idea that breaks in morphology are responsible for splitting the system into river and tide-dominated parts, similarly to the results obtained by *Sassi et al.* [2012]—in their case, however, they associated this separation with the point where the exponential width decrease stops. A jump in MWL also occurs around rkm 235, corresponding to the location of Lavolette Bridge, which acts as a major restriction to the flow. A fourth region can therefore be defined from this point, located near the entrance of Lake Saint-Pierre, up to Lanoraie where the semidiurnal tide completely extinguishes during neap tides. The sensitivity of MWL to variations in discharge considerably increases in the upstream region of the fluvial estuary, while it is little affected at the most downstream stations. Increases in tidal range are also reflected by increases in MWL, and vice versa, which is in accordance with the fortnightly rise and fall of MWL during spring and neap tides, respectively [LeBlond, 1979]. Further

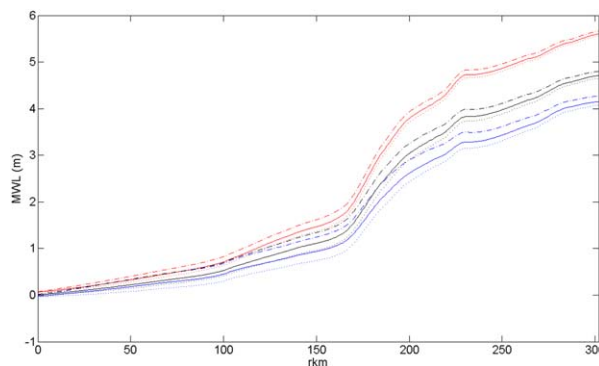


**Figure 9.** Longitudinal profiles of mean water levels (MWL) for quantiles of discharge and tidal range. Blue, black, and red lines correspond to 0.1, 0.5, and 0.9 quantiles of discharge, respectively; dotted, solid, and dash-dotted lines correspond to 0.1, 0.5, and 0.9 quantiles of tidal range, respectively.

modulations of the MWL induced by frictional interactions between tidal constituents are accounted for by the stage model through the range term. Moreover, the response of the system to variations in tidal range is greater at lower discharges. At downstream stations, MWL under conditions of low discharge and high tidal range are similar to MWL observed during high discharge and mean tidal range.

In Figures 10a and 10b, longitudinal profiles of amplitudes and phases are shown for the two dominant diurnal constituents,  $O_1$  and  $K_1$ . In general, they suggest a similar separation of the fluvial estuary into four distinct regions. Tidal amplitudes are

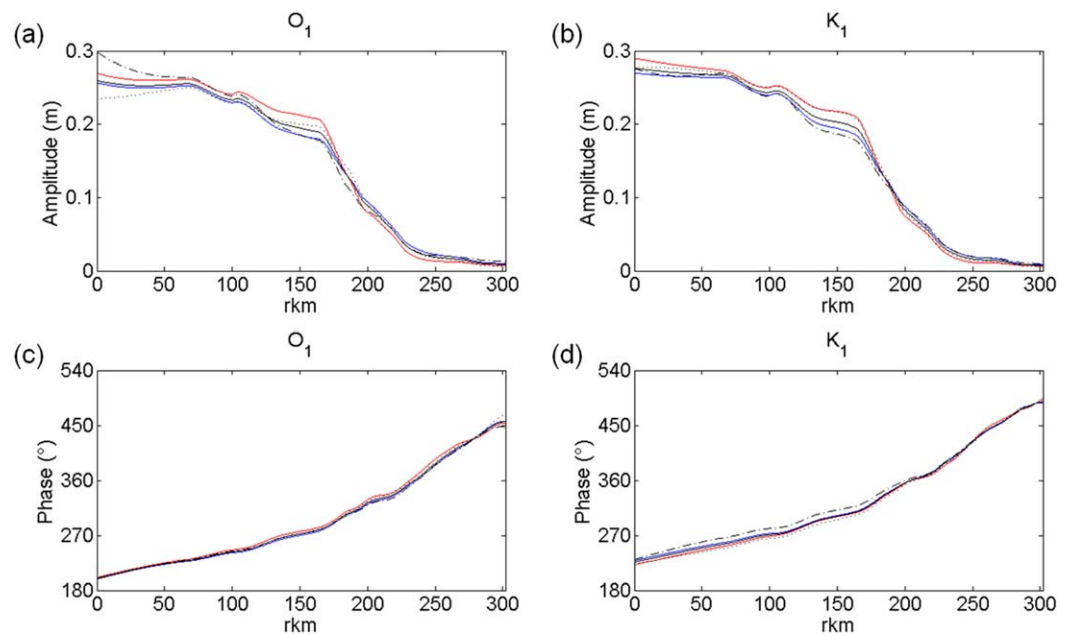


Figure 10. Same as Figure 9 for  $O_1$  and  $K_1$  amplitudes and phases.

characterized by a slow decrease downstream to Portneuf (rkm 163.5), followed by a sharp diminution upstream. At downstream stations, tidal amplitudes increase with discharge, because of larger water depth. Although amplitudes are being damped considerably from Portneuf, it is only around Cap-à-la-Roche (rkm 186) that tidal amplitudes start to decrease with increases in discharge. From that point, amplitudes are more severely damped by the discharge. Past the Laviollette Bridge (rkm 235), the decrease in tidal amplitudes slows as it approaches zero.

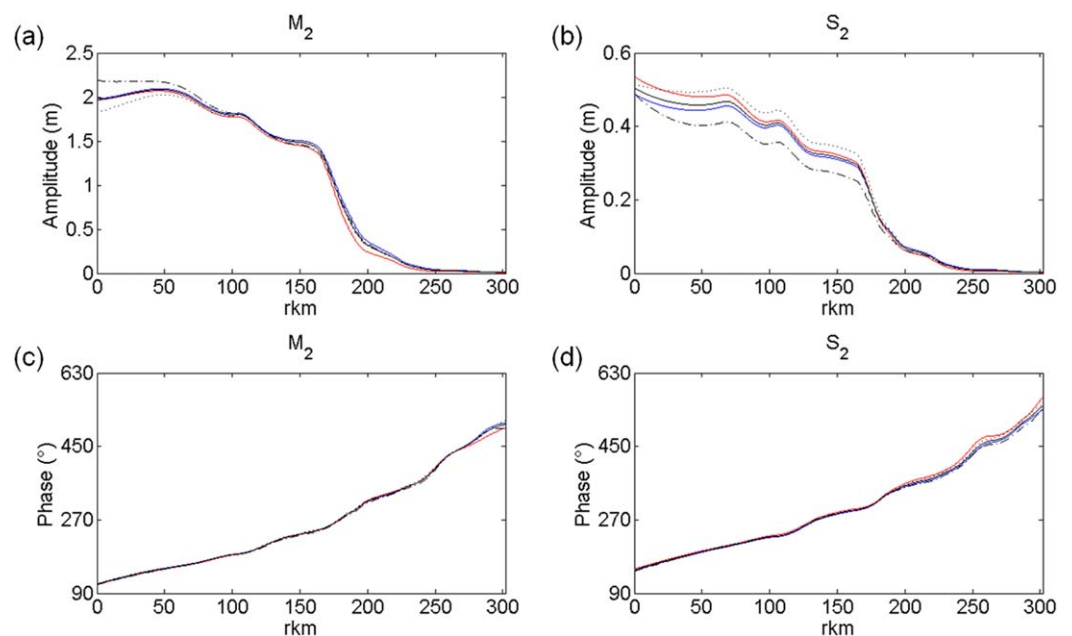
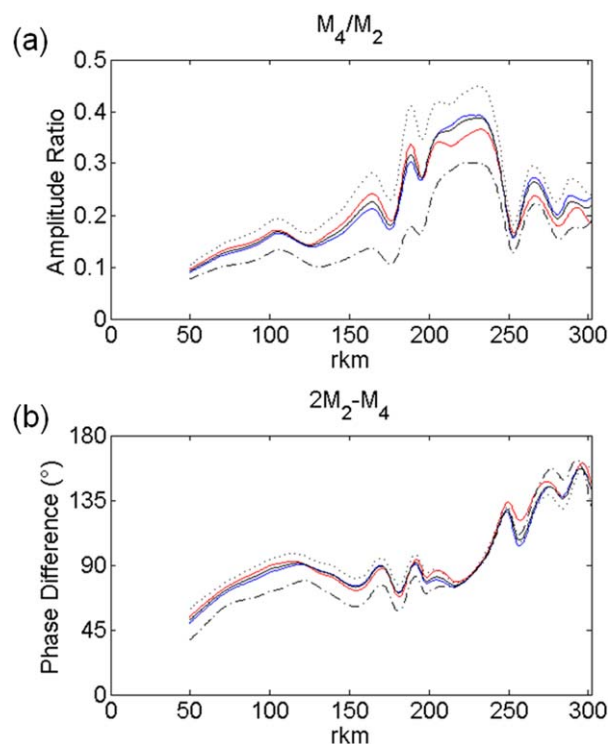


Figure 11. Same as Figure 10 for  $M_2$  and  $S_2$  amplitudes and phases.



**Figure 12.** Same as Figure 10 for  $M_4/M_2$  amplitude ratios and  $2M_2-M_4$  phase differences.

amplitudes are obtained at spring tides downstream of Portneuf (rkm 163.5), while they are lower upstream. This effect reverses upstream of Laviolette Bridge (rkm 235) in the case of  $O_1$  and upstream of Cap-à-la-Roche (rkm 186) for  $K_1$ .

As for the phases of  $O_1$  and  $K_1$  in Figures 10c and 10d, they show a constant increase with distance up to Portneuf (rkm 163.5) where a change in slope occurs, meaning that tide propagation is delayed due to the increasing influence of river flow (here a steeper slope means a slower propagation of the tidal wave). However, for  $O_1$ , phase lags are slightly larger at high discharges compared to low discharges, while the opposite is observed for  $K_1$ . Although this may be an artifact of the method, the consequence is a modification of their combined effect on a semimonthly basis. Finally, with larger tidal ranges the phases of both components are increased downstream while they are reduced upstream; this is another effect of the reversal of mean low waters during spring and neap tides.

In Figure 11, longitudinal profiles of amplitudes and phases are shown for the two dominant semidiurnal constituents,  $M_2$  and  $S_2$ . Similar observations as in Figure 10 can be made with respect to the general aspect of the curves. Both  $M_2$  and  $S_2$  show little variations in amplitude with discharge throughout the system, relative to their amplitude. Overall, slightly lower amplitudes are obtained at higher discharges with  $M_2$ , where damping is more influenced by discharge upstream of Portneuf (rkm 163.5). With  $S_2$ , higher amplitudes are observed downstream of Portneuf at higher discharges, while damping occurs upstream. The effects of tidal range on the amplitudes of  $M_2$  are little, except in the first  $\sim 80$  rkm, while the amplitudes of  $S_2$  are much more sensitive. In presence of larger tidal ranges, the amplitudes of  $S_2$  decrease, which might seem counter-intuitive. In fact,  $M_2$  and  $S_2$  interact together to produce neap-spring variations with a modulation period of 14.77 days. When tidal ranges are large (at spring tides),  $M_2$  and  $S_2$  are in phase, their amplitude being added to each other. However, as shown in Figure 11b, the individual amplitude of  $S_2$  is smaller during spring tide compared to neap tides, meaning that the summed amplitude of  $M_2$  and  $S_2$  is smaller than it would be in absence of friction. In other words,  $M_2$  and  $S_2$  are responsible for the generation of the neap-spring cycle, but they may be, in turn, affected by these fortnightly variations through friction, by a feedback mechanism.

$K_1$  is the dominant diurnal constituent and has higher amplitudes than  $O_1$  downstream of Portneuf. However, the amplitudes of  $O_1$  and  $K_1$  reach similar values around Portneuf,  $K_1$  being damped slightly more rapidly than  $O_1$ , possibly due to the higher frequency of  $K_1$  [Godin, 1999]. According to the development of the tidal potential [Doodson, 1921],  $O_1$  should consistently be smaller than  $K_1$ . One possible explanation for  $O_1$  and  $K_1$  being of similar amplitude is to attribute this discrepancy to the effect of  $M_2$  on  $K_1$  and  $O_1$  in presence of strong bottom friction [Godin and Martinez, 1994].

$O_1$  and  $K_1$  are responsible for the diurnal inequality associated with lunar declination. Their combined effect leads to a modulation with a period of 27.32 days, reaching a minimum every 13.66 days when the moon is over the equator. However, in presence of friction, their summed amplitude is also modulated by tidal range. In fact, taken individually, the amplitude of  $K_1$  is damped during spring tides (higher tidal range) and amplified during neap tides (lower tidal range) due to nonlinear interactions, as observed in Figure 10. As for  $O_1$ , higher

amplitudes are obtained at spring tides downstream of Portneuf (rkm 163.5), while they are lower upstream. This effect reverses upstream of Laviolette Bridge (rkm 235) in the case of  $O_1$  and upstream of Cap-à-la-Roche (rkm 186) for  $K_1$ .

As for the phases of  $O_1$  and  $K_1$  in Figures 10c and 10d, they show a constant increase with distance up to Portneuf (rkm 163.5) where a change in slope occurs, meaning that tide propagation is delayed due to the increasing influence of river flow (here a steeper slope means a slower propagation of the tidal wave). However, for  $O_1$ , phase lags are slightly larger at high discharges compared to low discharges, while the opposite is observed for  $K_1$ . Although this may be an artifact of the method, the consequence is a modification of their combined effect on a semimonthly basis. Finally, with larger tidal ranges the phases of both components are increased downstream while they are reduced upstream; this is another effect of the reversal of mean low waters during spring and neap tides.

In Figure 11, longitudinal profiles of amplitudes and phases are shown for the two dominant semidiurnal constituents,  $M_2$  and  $S_2$ . Similar observations as in Figure 10 can be made with respect to the general aspect of the curves. Both  $M_2$  and  $S_2$  show little variations in amplitude with discharge throughout the system, relative to their amplitude. Overall, slightly lower amplitudes are obtained at higher discharges with  $M_2$ , where damping is more influenced by discharge upstream of Portneuf (rkm 163.5). With  $S_2$ , higher amplitudes are observed downstream of Portneuf at higher discharges, while damping occurs upstream. The effects of tidal range on the amplitudes of  $M_2$  are little, except in the first  $\sim 80$  rkm, while the amplitudes of  $S_2$  are much more sensitive. In presence of larger tidal ranges, the amplitudes of  $S_2$  decrease, which might seem counter-intuitive. In fact,  $M_2$  and  $S_2$  interact together to produce neap-spring variations with a modulation period of 14.77 days. When tidal ranges are large (at spring tides),  $M_2$  and  $S_2$  are in phase, their amplitude being added to each other. However, as shown in Figure 11b, the individual amplitude of  $S_2$  is smaller during spring tide compared to neap tides, meaning that the summed amplitude of  $M_2$  and  $S_2$  is smaller than it would be in absence of friction. In other words,  $M_2$  and  $S_2$  are responsible for the generation of the neap-spring cycle, but they may be, in turn, affected by these fortnightly variations through friction, by a feedback mechanism.

As for the phases of  $M_2$  and  $S_2$ , shown in Figures 11c and 11d, variations are more subtle. Increases in discharge lead to slightly higher phases of  $S_2$ , while increases in tidal range lead to lower phases. Variations for  $M_2$  are almost imperceptible, but they show similar trends.

In upstream reaches of rivers, discharge has the effect of damping constituents of higher frequency more effectively [Godin, 1991; Godin and Martinez, 1994]. As a result, semidiurnal constituents are being damped faster than diurnal tides [see, e.g., Godin, 1999]. The decay profiles of the diurnal and semidiurnal components in Figures 10 and 11 between Saint-Joseph-de-la-Rive (rkm 0) and Lanoraie (rkm 302) are highly similar, but damping ratios seem to confirm this trend. In fact, for an average discharge, approximately 3% of the original diurnal amplitude remains at Lanoraie, while only 0.7% of the semidiurnal amplitude measured at Saint-Joseph-de-la-Rive is still observable at Lanoraie. While damping and phase speed may be frequency dependent, frictional nonlinearities also act as a generating mechanism for overtides and compound tides, hence contributing to the modification of the principal components.

In Figure 12 are shown the  $M_4/M_2$  amplitude ratios and  $2M_2-M_4$  phase differences as a function of upriver distance. The first 50 rkm were removed due to interpolation errors between the first two stations for frequencies higher or equal to that of  $M_4$  (see discussion in section 4). Other oscillations are most likely artifacts of the interpolation functions. In general, an increase in  $M_4/M_2$  amplitudes is observed up to Port Saint-François (rkm 241), indicating a transfer of energy from  $M_2$  to  $M_4$  through friction that is amplified upstream due to the increasing influence of discharge. The amplitude ratio then undergoes a rapid decrease in Lake Saint-Pierre as most of the tidal signal is damped,  $M_4$  being attenuated more rapidly than  $M_2$  due to its higher frequency. Similar observations can be made between scenarios of low and high discharge. Downstream of Cap-à-la-Roche (rkm 186), the  $M_4/M_2$  ratio increases with increasing discharges, while the reverse holds upstream. Past Cap-à-la-Roche,  $M_4$  is damped more rapidly by discharge than it is created from  $M_2$ , while downstream the energy transfer from  $M_2$  to  $M_4$  at higher discharge overcomes its damping effects.

As for tidal ranges, their effect on  $M_4/M_2$  amplitude ratio is consistent throughout the domain: a larger tidal range is expressed through smaller  $M_4/M_2$  ratios, and vice versa. This is counterintuitive at first sight, as increases in the  $M_4/M_2$  ratio are generally expected at spring tide rather than neap tide. One possible explanation is that the relative decrease in amplitude of  $M_4$ , even more pronounced than that of  $M_2$  during spring tide, may be related to the lowering of low waters at neap tides rather than spring tides, with correspondingly stronger bottom friction.

The key to explain this unusual observation may lie in the tidal analysis approach used and in how river tides are conceptualized. For example, CWT tidal analysis methods [Jay and Flinchem, 1997, 1999; Jay and Kukulka, 2003; Buschman et al., 2009] are able to express time variations in the tidal content of a signal, although with no distinction between frequencies of a given tidal band. Ratios of  $D_4/D_2$  amplitudes (where  $D_2$  and  $D_4$  refer to the semidiurnal and quarter-diurnal species, respectively) thus represent the relative energy contained in the quarter-diurnal and semidiurnal bands, all frequencies combined. Similarly, the concept of "reduced vector" introduced by George and Simon [1984], and notably applied by Godin [1999], yields daily averaged band estimates of the major tidal components, again with no possible separation between neighbouring frequencies. The amplitudes associated with  $M_2$  and  $M_4$  thus correspond to the total energy of their respective tidal band, much like CWT. Because NS\_TIDE allows for the inclusion of multiple frequencies within each tidal band, direct comparisons with conventional methods is not straightforward. In fact, to actually reproduce the variations in  $M_4/M_2$  ratios as traditionally expected from conventional methods, the total contribution from quarter-diurnal and semidiurnal bands needs to be taken into account. For example, plots of the dominant semidiurnal and quarter-diurnal constituents (not shown) confirm that their summed amplitudes in each tidal band are synchronized with tidal range, and so are the amplitude ratios. This is because both fortnightly and monthly modulations are induced by the interactions between pairs of frequencies. Taken individually, however, these constituents may respond differently to changes in discharge and ocean tidal range. Moreover, the energy transfer through friction from  $M_2$  to higher frequencies not only involves  $M_4$ , but also  $MN_4$ ,  $MS_4$ , and so on. As such, results are dependent on the number of included constituents within each tidal band.

Finally, in Figure 12b, the  $2M_2-M_4$  phase differences show a gradual increase as a function of upriver distance. The relative phase differences are below  $180^\circ$ , which indicates a flood tidal asymmetry [Friedrichs and

Aubrey, 1988]. As these differences approach  $180^\circ$ , tidal asymmetry increases, with a signal characterized by short and abrupt flood tides and slowly decreasing ebb tides. The phase differences tend to increase with discharge, except for stations located between Neuville (rkm 138) and Cap-à-la-Roche (rkm 186); this is not clear whether it is the result of interpolations or river-tide interactions. Moreover, in the first  $\sim 250$  rkm, flood tidal asymmetry is enhanced during neap tides compared to spring tides, which is coherent with the variations in  $M_4/M_2$  ratios. The other quarter-diurnal tides possibly play a role in reinforcing tidal asymmetry.

#### 4. Discussion and Conclusion

The potential of NS\_TIDE to predict tides in upstream reaches of tidal rivers has been demonstrated. Signal analyses from 13 contrasting stations in terms of tidal-fluvial dynamics showed significantly better statistics than classical HA at upstream stations, while model performance at downstream stations was comparable to classical HA. Despite all assumptions made on the physics, the predicting capability of NS\_TIDE was surprisingly high. In fact, many parameters such as the model exponents were set to constant values, while in reality they may be influenced by the river geometry, including the cross-sectional area, the wetted perimeter, the convergence rate, or other factors. Furthermore, the model implemented in NS\_TIDE was developed for systems where tidal and fluvial flows are of similar magnitude. Knowing that tidal discharges can be more than 5 times greater than the residual flow at downstream locations, the agreement between the predicted and the observed water levels is remarkable. Even with these simplifications, tidal-fluvial processes that are explained by the method are physically plausible. When time-averaged, the amplitudes and phases resemble those obtained from HA, which confirms that the energy is well distributed between the constituents. Furthermore, predicting water levels from hindcast results for a time period other than the analysis period [e.g., *Matte et al.*, 2013], or equivalently, at intermediate stations if coefficients are spatially interpolated (like here), is a good way to test the validity of a model. Nonphysical variations (e.g., unreal amplitudes and phases), which sometimes improve the harmonic fits, are likely to degrade the predictions when transposed to other time periods or stations. Here the addition of constituents in the analysis was carried out until the point was reached where prediction accuracy decreased or artifacts started to appear (e.g., incoherent phases compared to classical HA). While resolving for too few components could lead to oscillations in the tidal amplitudes, some of the modulations observed in the results for the dominant frequencies were not eliminated by adding more constituents. The remaining variations may be attributable to increased errors under specific discharge and tidal range conditions, or they may be of physical origin. Further investigation may be needed to identify the sources of variation.

The model was validated with observations at a total of 32 stations and by comparison with the operational ONE-D model of the St. Lawrence River. Better statistics were obtained with the ONE-D model, but at the price of a more complex and time-consuming modeling process (including the time devoted to develop and calibrate the model). In contrast, NS\_TIDE provided still very good accuracy from a simpler but more informative model in terms of tidal-fluvial dynamics. In fact, numerical models and tidal analysis tools have very different strengths and weaknesses. Much can be learned from the existing operational model, especially if all terms in the momentum balance can be stored. However, no information on the time-varying frequency content of water levels or velocities can be obtained if not combined with other tidal analysis methods. By contrast, NS\_TIDE uses a functional representation of tides (i.e., constituent amplitudes and phases) expressed in terms of external nonstationary forcing, which can be used for prediction in a straightforward manner. With an approach based on regression analysis, no field description is needed (topography, substrate friction, etc.), thus minimizing sensitivity to local topographic or frictional uncertainty. Instead, model parameters are optimized by stations to account for changes in these variables, as experienced by the water levels. NS\_TIDE also preserves the compactness and efficiency of HA and ensures continuity between analyses performed in the St. Lawrence fluvial estuary, marine estuary, and gulf. Furthermore, its capacity to distinguish frequencies within tidal species represents a considerable improvement compared to conventional tidal analysis methods that offers new possibilities for dynamical inquiry.

In NS\_TIDE, the inclusion of river discharge in the basis function drastically improves the predictions at upstream stations, which had been demonstrated before, notably by *Godin* [1985, 1999] and *Jay and Flinchem* [1997]. Similar adaptations of the models developed by *Kukulka and Jay* [2003a, 2003b] were made to hindcast lower low water (LLW) and higher high water (HHW) as a function of river flow and external tidal

forcing in the Columbia River [Jay *et al.*, 2011]. Likewise, an inverse model based on analysis of tidal statistics was derived from Kukulka and Jay's [2003a, 2003b] approach to produce monthly averaged tidal discharge estimates in the San Francisco Bay [Moftakhari *et al.*, 2013]; in their analysis, however, the tidal range term was neglected, because of the 31.7 day averaging period used.

Buschman *et al.* [2009] presented a method to analyze subtidal water levels in tidal rivers. Unlike Kukulka and Jay's [2003a, 2003b] models, they used Godin's approximation of the friction term [Godin, 1999], rather than the Tschebyshev polynomial approach [Dronkers, 1964], to derive a new expression for subtidal friction, and successfully applied their model in the Berau River (Indonesia). They attribute subtidal motion to three sources, namely the river flow, river-tide interactions, and tides alone. The river-tide interaction was mainly responsible for fortnightly variations in water levels at the station under study. By comparison, the stage model implemented in NS\_TIDE, derived from Kukulka and Jay's [2003b] model, decompose variations in MWL into contributions from river forcing, tides, atmospheric pressure (not included here), and topographic offset. As shown in the present application, NS\_TIDE is able to reproduce the nonlinearly generated fortnightly variations in MWL, as well as seasonal variations associated with river discharge. The frequency content of the stage model contains energy at annual and semiannual periods due to seasonal cycles in discharge ( $c_1$  term), and at monthly and semimonthly periods due to the influence of the tidal range ( $c_2$  term). These low frequencies are generated by tidal-fluvial interactions and nonlinear compound tides, which are inadequately represented in tidal rivers by the usual harmonic apparatus [Parker, 2007; Matte *et al.*, 2013]. The improved statistics in the upstream reach of the St. Lawrence fluvial estuary (cf. Figure 5) is directly related to the ability of the stage model to accurately represent subharmonics.

Part of the error in the spatial model is related to the position of the analysis stations, the distance that separates them and the interpolation functions used. It was shown that Hermite polynomials are good interpolators in the present case, given the spatial variations in the coefficients in the St. Lawrence. However, as the frequency of the constituents increases, the wavelength decreases, leading to more oscillations in the coefficients due to a higher number of cycles. When the distance separating the stations approaches half the wavelength of the constituent, interpolation errors may increase drastically. In that case, components of higher frequencies should be neglected or more stations should be added to the available network. In the present application, the average distance between the stations is 25 km (cf. Table 1), which is less than half the wavelength of  $M_8$  (roughly  $\sim 70$  km). Between Saint-Joseph-de-la-Rive (rkm 0) and Saint-François (rkm 66), however, the interpolation of  $M_4$  (wavelength  $\sim 140$  km) and higher frequencies is questionable due to the distance separating the two stations, as mentioned above (cf. Figure 12). Using numerical models to improve the interpolation, by taking advantage of a higher spatial resolution, may be an interesting avenue to explore.

NS\_TIDE does not currently differentiate between the rising and falling limbs of a hydrograph, mainly because coefficients determined by regression are constant in time. This feature allows general applicability of the model, although it cannot account for hysteresis phenomena. For example, as shown by Sassi and Hoitink [2013], tides are damped faster during the rising limb of a discharge wave than inversely. The fact that nonstationary (rather than constant) river discharges are built directly in the basis function matrix of NS\_TIDE offers the possibility of analysing such mechanisms; they should be addressed in the future. Moreover, recent studies show that flow division in tidal branching systems is controlled by river flow, tides, and the interactions between the two [Buschman *et al.*, 2010; Sassi *et al.*, 2011]. Notably, the discharge asymmetry features fortnightly oscillations attributable to neap-spring variations in tidal range. The use of NS\_TIDE to further examine these interactions would be interesting, especially at the junction of Orleans Island in the St. Lawrence fluvial estuary.

The spatial, nonstationary harmonic model presented in this paper represents a new way to look at river tides. Applied to the St. Lawrence fluvial estuary, it successfully reproduced stage and tidal properties in an unprecedented way, by expressing their variations in terms of nonstationary forcing variables, i.e., river discharge and ocean tidal range, for a broad range of conditions. Several characteristics of the St. Lawrence and, by extension, of tidal rivers in general were brought to light by the model. They can be summarized as follows:

1. The decrease in predictive skill of classical HA compared to NS\_TIDE coincides with a break in river morphology, in the present case associated with the presence of rapids combined with a rapid increase of the bottom slope, which marks the transition from the tidal to tidal-fluvial regimes.

2. A mean water level setup is observed, starting in the transition zone between the tidal and tidal-fluvial regimes (Portneuf; rkm 163.5).
3. The sensitivity of mean water levels to variations in discharge considerably increases upstream. The response of the system to variations in tidal range is greater at lower discharges.
4. A fortnightly rise and fall of the mean water levels is observed during spring and neap tides, respectively. The amplitude of the fortnightly wave reaches a maximum as it enters into the tidal-fluvial regime (Cap-à-la-Roche; rkm 186).
5. Tides are rapidly damped in the transition zone between the tidal and tidal-fluvial regimes, and tide propagation is delayed.
6. The response of tidal constituents to external forcing by discharge and ocean tides is both spatially and frequency dependent; it differs between constituents in different tidal species, but also between frequencies of a single species.
7. Frictional nonlinearities act as a generating mechanism for overtides, until they reach a point upstream where they are damped more rapidly by friction than they are generated through nonlinear interactions.

Together with numerical modeling, nonstationary HA has the potential to improve current knowledge on tidal-fluvial processes in highly nonlinear environments such as tidal rivers, pushing the limits of conventional tidal prediction tools. Furthermore, it can be used to assess the temporal and spatial variability of tidal-fluvial dynamics in systems where the development of a numerical model is not possible.

#### Acknowledgments

This work was supported by scholarships from the Natural Sciences and Engineering Research Council of Canada and Fonds de recherche du Québec–Nature et technologies. The authors wish to thank Denis Lefavre and Alain D'Astous for providing simulation results from the ONE-D model, David A. Jay for discussions regarding the analysis of tides in rivers, and two anonymous reviewers for their constructive comments on the manuscript.

#### References

- Amin, M. (1983), On perturbations of harmonic constants in the Thames Estuary, *Geophys. J. R. Astron. Soc.*, *73*(3), 587–603.
- Amin, M. (1985), Temporal variations of tides on the west coast of Great Britain, *Geophys. J. R. Astron. Soc.*, *82*(2), 279–299.
- Amin, M. (1993), The mutual influence of tidal constituents in the presence of bottom stress, *Estuarine Coastal Shelf Sci.*, *37*(6), 625–633.
- Bouchard, A., and J. Morin (2000), Reconstitution des débits du fleuve Saint-Laurent entre 1932 et 1998, *Rapp. Tech. RT-101*, 71 p., Environ. Can., Sainte-Foy.
- Buschman, F. A., A. J. F. Hoitink, M. van der Vegt, and P. Hoekstra (2009), Subtidal water level variation controlled by river flow and tides, *Water Resour. Res.*, *45*, W10420, doi:10.1029/2009WR008167.
- Buschman, F. A., A. J. F. Hoitink, M. van der Vegt, and P. Hoekstra (2010), Subtidal flow division at a shallow tidal junction, *Water Resour. Res.*, *46*, W12515, doi:10.1029/2010WR009266.
- Codiga, D. L. (2011), Unified tidal analysis and prediction using the UTide Matlab functions, *Tech. Rep. 2011-01*, 59 p., Grad. Sch. of Oceanogr., Univ. of R. I., Narragansett.
- Côté, J.-P., and J. Morin (2007), Principales interventions humaines survenues dans le fleuve Saint-Laurent entre Montréal et Québec au 20e siècle: 1907–2005, *Rapp. Tech. RT-141*, 65 p., Environ. Can., Sainte-Foy.
- Couillard, D. (1987), Qualité des sédiments en suspension et de fond du système Saint-Laurent (Canada), *Hydrol. Sci. J.*, *32*(4), 445–467.
- Dailey, J. E., and D. R. F. Harleman (1972), Numerical model for the prediction of transient water quality in estuary networks, *RT72-72*, *Rep. 158*, 226 pp., Hydrodyn. Lab., Mass. Inst. of Technol., Cambridge, Mass.
- Doodson, A. T. (1921), The harmonic development of the tide-generating potential, *Proc. R. Soc. London, Ser. A*, *100*(704), 305–329.
- Dronkers, J. J. (1964), *Tidal Computations in Rivers and Coastal Waters*, 518 p., North-Holland, Amsterdam.
- El-Sabh, M. I., and T. S. Murty (1990), Mathematical modelling of tides in the St. Lawrence Estuary, in *Oceanography of a Large-Scale Estuarine System: The St. Lawrence*, edited by M. I. El-Sabh and N. Silverberg, pp. 10–50, Springer, N. Y.
- Flinchem, E. P., and D. A. Jay (2000), An introduction to wavelet transform tidal analysis methods, *Estuarine Coastal Shelf Sci.*, *51*(2), 177–200.
- Foreman, M. G. G., J. Y. Cherniawsky, and V. A. Ballantyne (2009), Versatile harmonic tidal analysis: Improvements and applications, *J. Atmos. Oceanic Technol.*, *26*(4), 806–817.
- Friedrichs, C. T., and D. G. Aubrey (1988), Non-linear tidal distortion in shallow well-mixed estuaries: A synthesis, *Estuarine Coastal Shelf Sci.*, *27*(5), 521–545.
- Fritsch, F., and R. Carlson (1980), Monotone piecewise cubic interpolation, *SIAM J. Numer. Anal.*, *17*(2), 238–246.
- Gagnon, M. (1995), *Bilan Régional—Québec-Lévis. Zone d'Intervention Prioritaire 14*, 65 p., Environ. Can-Région du Québec, Cent. Saint-Laurent, Montréal, Qué., Canada.
- Gallo, M. N., and S. B. Vinzon (2005), Generation of overtides and compound tides in Amazon estuary, *Ocean Dyn.*, *55*(5–6), 441–448.
- George, K. J., and B. Simon (1984), The species concordance method of tide predictions in estuaries, *Int. Hydrogr. Rev.*, *61*(1), 121–145.
- Godin, G. (1972), *The Analysis of Tides*, 264 pp., Univ. of Toronto Press, Toronto, Ont., Canada.
- Godin, G. (1984), The tide in rivers, *Int. Hydrogr. Rev.*, *61*, 159–170.
- Godin, G. (1985), Modification of river tides by the discharge, *J. Waterway Port Coastal Ocean Eng.*, *111*(2), 257–274.
- Godin, G. (1991), Compact approximations to the bottom friction term, for the study of tides propagating in channels, *Cont. Shelf Res.*, *11*(7), 579–589.
- Godin, G. (1999), The propagation of tides up rivers with special considerations on the Upper Saint Lawrence River, *Estuarine Coastal Shelf Sci.*, *48*(3), 307–324.
- Godin, G., and A. Martinez (1994), Numerical experiments to investigate the effects of quadratic friction on the propagation of tides in a channel, *Cont. Shelf Res.*, *14*(7–8), 723–748.
- Hicks, F. (1997), Accuracy and conservation characteristics of the numerical algorithm in Environment Canada's ONE-D model, *Can. J. Civ. Eng.*, *24*(4), 560–569.

- Holland, P. W., and R. E. Welsch (1977), Robust regression using iteratively reweighted least-squares, *Commun. Stat. Theory Methods*, 6(9), 813–827.
- Huber, P. J. (1996), Robust statistical procedures, in *CBMS-NSF Regional Conference Series in Applied Mathematics*, 67 p., Soc. of Ind. and Appl. Math., Bayreuth, Germany.
- Jay, D. A. (1991), Green's law revisited: Tidal long wave propagation in channels with strong topography, *J. Geophys. Res.*, 96(20), 585–598.
- Jay, D. A., and E. P. Flinchem (1997), Interaction of fluctuating river flow with a barotropic tide: A demonstration of wavelet tidal analysis methods, *J. Geophys. Res.*, 102(C3), 5705–5720.
- Jay, D. A., and E. P. Flinchem (1999), A comparison of methods for analysis of tidal records containing multi-scale non-tidal background energy, *Cont. Shelf Res.*, 19(13), 1695–1732.
- Jay, D. A., and T. Kukulka (2003), Revising the paradigm of tidal analysis—The uses of non-stationary data, *Ocean Dyn.*, 53(3), 110–125.
- Jay, D. A., K. Leffler, and S. Degens (2011), Long-term evolution of Columbia River tides, *J. Waterway Port Coastal Ocean Eng.*, 137(4), 182–191.
- Kukulka, T., and D. A. Jay (2003a), Impacts of Columbia River discharge on salmonid habitat: 1. A nonstationary fluvial tide model, *J. Geophys. Res.*, 108(C9), 3293, doi:10.1029/2002JC001382.
- Kukulka, T., and D. A. Jay (2003b), Impacts of Columbia River discharge on salmonid habitat: 2. Changes in shallow-water habitat, *J. Geophys. Res.*, 108(C9), 3294, doi:10.1029/2003JC001829.
- LeBlond, P. H. (1978), On tidal propagation in shallow rivers, *J. Geophys. Res.*, 83(C9), 4717–4721.
- LeBlond, P. H. (1979), Forced fortnightly tides in shallow rivers, *Atmos. Ocean*, 17(3), 253–264.
- LeBlond, P. H. (1991), Tides and their interactions with other oceanographic phenomena in shallow water (Review), in *Tidal Hydrodynamics*, edited by B. B. Parker, pp. 357–378, John Wiley, N. Y.
- Lefavre, D., S. Hamdi, and B. Morse (2009), Statistical analysis of the 30-day water level forecasts in the St. Lawrence River, *Mar. Geod.*, 32(1), 30–41.
- Leffler, K. E., and D. A. Jay (2009), Enhancing tidal harmonic analysis: Robust (hybrid  $L^1/L^2$ ) solutions, *Cont. Shelf Res.*, 29(1), 78–88.
- Martin, P. J., S. R. Smith, P. G. Posey, G. M. Dawson, and S. H. Riedlinger (2009), Use of the Oregon State University tidal inversion software (OTIS) to generate improved tidal prediction in the East-Asian Seas, *Rep. NRL/MR/7320-09-9176*, 29 p., Nav. Res. Lab., Stennis Space Cent., Bay St. Louis, Miss.
- Matte, P., D. A. Jay, and E. D. Zaron (2013), Adaptation of classical tidal harmonic analysis to nonstationary tides, with application to river tides, *J. Atmos. Oceanic Technol.*, 30(3), 569–589.
- Matte, P., Y. Secretan, and J. Morin (2014), Quantifying lateral and intratidal variability in water level and velocity in a tide-dominated river using combined RTK GPS and ADCP measurements, *Limnol. Oceanogr. Methods*, 12, 279–300.
- Moftakhari, H. R., D. A. Jay, S. A. Talke, T. Kukulka, and P. D. Bromirski (2013), A novel approach to flow estimation in tidal rivers, *Water Resour. Res.*, 49, 4817–4832.
- Morse, B. (1990), *St-Lawrence River Water-Levels Study: Application of the ONE-D Hydrodynamic Model*, Transp. Canada, Waterways Dev. Div., Can. Coast Guard., Ottawa, Ont., Canada.
- Munk, W. H., B. Zetler, and G. W. Groves (1965), Tidal cusps, *Geophys. J. R. Astron. Soc.*, 10(2), 211–219.
- Nidziko, N. J. (2010), Tidal asymmetry in estuaries with mixed semidiurnal/diurnal tides, *J. Geophys. Res.*, 115, C08006, doi:10.1029/2009JC005864.
- Park, S.-Y., D.-S. Byun, and D. Hart (2012), A solution for the correct interpolation of data across regions with abrupt changes in tidal phase-lag, *Ocean Sci. J.*, 47(3), 215–219.
- Parker, B. B. (1991), The relative importance of the various nonlinear mechanisms in a wide range of tidal interactions (Review), in *Tidal Hydrodynamics*, edited by B. B. Parker, pp. 237–268, John Wiley, N. Y.
- Parker, B. B. (2007), Tidal analysis and prediction, *Rep. NOS CO-OPS 3*, 378 p., U.S. Dep. of Commer., Silver Spring, Md.
- Pawlowicz, R., B. Beardsley, and S. Lentz (2002), Classical tidal harmonic analysis including error estimates in MATLAB using T\_TIDE, *Comput. Geosci.*, 28(8), 929–937.
- Robitaille, J. (1998a), *Bilan Régional—Pointe-du-Lac-Deschambault. Zone d'Intervention Prioritaire 12*, 90 p., Environ. Can.-Région du Québec, Conserv. de l'environ., Cent. Saint-Laurent, Montréal, Qué., Canada.
- Robitaille, J. (1998b), *Bilan Régional—Portneuf-Saint-Nicolas. Zone d'Intervention Prioritaire 13*, 78 p., Environ. Can.-Région du Québec, Conserv. de l'Environ., Cent. Saint-Laurent, Montréal, Qué., Canada.
- Sassi, M. G., and A. J. F. Hoitink (2013), River flow controls on tides and tide-mean water level profiles in a tidal freshwater river, *J. Geophys. Res. Oceans*, 118, 4139–4151, doi:10.1002/jgrc.20297.
- Sassi, M. G., A. Hoitink, B. de Brye, B. Vermeulen, and E. Deleersnijder (2011), Tidal impact on the division of river discharge over distributary channels in the Mahakam Delta, *Ocean Dyn.*, 61(12), 2211–2228.
- Sassi, M. G., A. J. F. Hoitink, B. de Brye, and E. Deleersnijder (2012), Downstream hydraulic geometry of a tidally influenced river delta, *J. Geophys. Res.*, 117, F04022, doi:10.1029/2012JF002448.
- Shaw, A. G. P., and M. N. Tsimplis (2010), The 18.6 yr nodal modulation in the tides of Southern European coasts, *Cont. Shelf Res.*, 30(2), 138–151.